Effect of Fe Doping on The Structural, Morphological, Optical, Magnetic and Dielectric Properties of BaSnO3

Jibi John
University of Kerala
Suresh S
University of Kerala
Savitha Pillai S
University of Kerala
Reji Philip
Raman Research Institute
V. P. Mahadevan Pillai (vpmpillai9@gmail.com)
University of Kerala https://orcid.org/0000-0002-5856-2319

Research Article

Keywords: Perovskite oxide, Rietvield refinement, Hexagonal nanorods, Optical limiting behavior, Ferromagnetic order

Posted Date: February 15th, 2021

DOI: https://doi.org/10.21203/rs.3.rs-193316/v1

Version of Record: A version of this preprint was published at Journal of Materials Science: Materials in Electronics on April 18th, 2021. See the published version at https://doi.org/10.1007/s10854-021-05806-9.

Effect of Fe doping on the structural, morphological, optical, magnetic and dielectric properties of $BaSnO_3$

*Jibi John[1], Suresh S [1,2], Savitha Pillai.S[3], Reji Philip[4]and V.P. Mahadevan Pillai[1]**
[1]*Department of Optoelectronics, University of Kerala, Kariavattom 695581, Thiruvanthapuram, Kerala, India.*
[2]*Department of Electronics, SreeAyyappa College, Eramallikkara, Chengannur, Kerala, India*
[3]*Department of Physics, University of Kerala, Kariavattom*
[4]*Light and Matter Physics Group, Raman Research Institute, Bangalore 560080, India*
** E-mail:vpmpillai9@gmail.com*

Abstract

Doping at the possible A or B site in the ABO_3 perovskite can alter the structural, morphological and optical properties of the compounds. Perovskite alkaline earth stannate $BaSnO_3$ doped with Fe resulted in $BaSn_{1-x}Fe_xO_3$ compounds having different concentrations (x=0.00, 0.01, 0.02, 0.03, 0.05 and 0.07) were prepared by solid-state method. The Rietveld analyzes were performed to determine the phase purity and the changes in structural parameters. Morphological analysis identifies the formation of hexagonal nanorods with doping. The non linear optical property of the prepared samples shows optical power limiting behaviour. Magnetic property signifies the existence of ferromagnetic order and EPR studies reveal the possible ferromagnetic ordering of Fe doped samples. Dielectric loss decreases with Fe doping and has a gradual decrease in the higher frequency regime and has applications in high frequency devices.

Key words: Perovskite oxide, Rietvield refinement, Hexagonal nanorods, Optical limiting behavior, Ferromagnetic order.

1. Introduction

Alkaline-earth stannates belong to the perovskite-type oxides having the general formula $ASnO_3$ (A = Ba, Sr, Ca) have attracted considerable attention nowadays due to their interesting physical properties such as high optical transparency, photocatalytic activity, ferroelectricity, superconductivity, and magnetism [1-4]. Among various perovskites, $BaSnO_3$ is a semiconductor with a cubic structure having a wide bandgap of 3.4 eV [5,6]. It can remain stable even at high temperatures [7]. $BaSnO_3$ has been found applications in thermally stable capacitors, dye-

sensitized solar cells, photocatalyst, humidity sensors and gas sensors [8-10]. Appropriate doping in $BaSnO_3$ leads to interesting magnetic, semiconducting and ferroelectric properties [11]. The partial substitution at the cationic and the anionic sites leads to a change in the properties while preserving the perovskite structure [12]. The oxygen vacancies are common in these structures which in turn affect the physio-chemical properties of materials [13]. The dopant atoms at Ba^{2+} and Sn^{4+} cationic sites will enhance in the physical properties and also cause a change in the octahedral tilting of the perovskite structure. Upadyay et al., doped La on $BaSnO_3$ at Ba site and found that there is a decrease in the lattice parameter and grain size with increase in lanthanum doping concentration [14]. They attributed the conduction and dielectric relaxation to hopping of electrons among Sn^{2+} or Sn^{3+} and Sn^{4+} ions [14]. High electrical mobility of 320 $cm^2(Vs)^{-1}$ at room temperature and superior thermal stability at high temperatures is reported in La doped $BaSnO_3$ [15]. The reduction in the bandgap of Co-doped $BaSnO_3$is ascribed due to the crystallite size variation and defects such as oxygen vacancies [16]. Due to the capability of doping in A and B sites, high electron mobility and oxygen stability, $BaSnO_3$ has large potential applications as a system to combine the versatile perovskite structure and the semiconductor technologies [17].

Moura et al., reported that Fe doping decreased the bandgap energy of $BaSnO_3$ and favored the photocatalytic reaction due to the formation of intermediate levels inside the bandgap [18].The observation of ferromagnetism in Mn and Fe-doped $BaSnO_3$ is an important leap in the literature that opened up the path for $BaSnO_3$ dilute magnetic semiconductor (DMS) applications [11, 22]. DMS are formed when a small quantity of magnetic ions are doped with semiconductors. The utilization of spin and charges of electrons in the DMS materials have attracted in the application of spintronic devices [11]. The magnetic properties of Cr doped $BaSnO_3$ nanostructures synthesized by chemical precipitation method has showed a change from diamagnetic to ferromagnetic behavior [23]. Manju et al., reported the effect of Fe/Co ions on the structural and magnetic properties of $BaSnO_3$ nanoparticles and found that the ferromagnetic property varies gradually with increase in substitution of Co content. [24]. James et al., reported that the presence of oxygen vacancies, structural deformation and surface morphology of Fe doped $BaSnO_3$ have improved the magnetic properties of $BaSnO_3$ [19]. Licheron et al., reported a superconducting behavior of $Ba(Sn_{0.7}Sb_{0.3})O_3$ sample [20]. Singh et al., reported the dielectric properties of La doped $BaSnO_3$ and found that the remnant polarization and the coercive field

decreases with increase of La in the lattice [21]. To the best of our knowledge, detailed structural analysis using the Rietveld analysis of XRD, and measurement of nonlinear optical absorption and dielectric properties, are not reported so far for Fe doped $BaSnO_3$.

There are different methods for the preparation of $BaSnO_3$. Many preparation methods were reported to obtain nanoparticles of $BaSnO_3$ with cubic perovskite structure such as sol-gel method [25] hydrothermal method [26] and modified combustion technique [27] etc. In the present work, $BaSn_{1-x}Fe_xO_3$ (x =0, 0.01, 0.02, 0.03, 0.05 and 0.07) compounds were prepared by the solid-state reaction method, and the structural, morphological, optical, electronic and their magnetic properties have been investigated in detail.

2. Experimental Details

The powder samples of pure $BaSnO_3$ and doped $BaSn_{1-x}Fe_xO_3$ (x=1, 2, 3, 5 and 7 mol % concentration) were synthesized by solid-state reaction method. $BaCO_3$, SnO_2 and Fe_2O_3 powders (Sigma, purity-99.99%) were taken in stoichiometric ratio and is mixed using an agate mortar and pestle. The mixture is then grinded well-using acetone as the mixing media. The powder thus grinded was taken in a platinum crucible and is heated at a temperature of 1250 $^{\circ}$C in a programmable furnace for 6 h at a rate 5 $^{\circ}$C min^{-1} and was allowed to cool down naturally to room temperature. To ensure the complete reaction, these mixtures were again milled and further heated at a temperature of 1250 $^{\circ}$C for 6h. The prepared Fe doped $BaSnO_3$ samples with x = 0.00, 0.01, 0.02, 0.03, 0.05 and 0.07 are denoted as BF0, BF1, BF2, BF3, BF5 and BF7 respectively. The synthesized pure $BaSnO_3$ and Fe doped $BaSnO_3$samples were analyzed by different characterization techniques. The crystalline purity of the prepared samples was characterized by the Bruker Advance 8 XRD diffractometer. The XRD pattern was recorded using Cu-$K\alpha_L$ radiation of wavelength 1.5406 Å and at a scan speed of 2° min^{-1} in the 2θ range 20-80°with a step size of 0.04°. FTIR spectra were recorded by Perkin Elmer FT-IR/FIR Frontier Spectrometer in the frequency range of 400- 4000 cm^{-1}. Micro-Raman spectra of the synthesized powders were recorded with excitation radiation of a wavelength of 633 nm from a helium ion laser using Labram- HR 800 spectrometer (Horiba JobinYvon) equipped with Synapse CCD camera system maintained at -70 $^{\circ}$C having a spectral resolution of about 1 cm^{-1}. Nova Nano SEM-450 Field Emission Scanning Electron Microscope (FEI- USA) was used for analyzing the surface morphology of the synthesized samples. Perkin Elmier Lambda 950 spectrophotometer

was used for capturing the UV-Visible spectrum in the wavelength range of 2300–250 nm. Open aperture Z-scan experiments were done using a frequency doubled Q-switched Nd:YAG laser of wavelength 532 nm for measuring the third order nonlinear absorption coefficient. Magnetic properties were studied using a Lakeshore 7410S Vibrating Sample Magnetometer (VSM) of sensitivity 10^{-7} emu and magnetic field resolution of ± 0.001%. Electron spin resonance studies were performed at X-band, 9.5 GHz (JEOL, Model:FA200). The dielectric properties of the pure and Fe doped compounds were studied using HIOKI3532-50LCR Hi TESTER.

3. Results and Discussion

3.1 XRD Analysis

Fig.1(a) shows the XRD patterns of the $BaSn_{1-x}Fe_xO_3$ (x=0.00, 0.01, 0.02,0.03, 0.05 and 0.07) prepared by solid-state method. The XRD patterns of pure $BaSnO_3$ and Fe doped $BaSnO_3$ samples consist of six peaks which are indexed to (110), (111), (200), (211), (200) and (310)lattice ref planes of cubic $BaSnO_3$ perovskite structure with space group *Pm*3*m*. All the peaks in the diffraction patterns are well-matched with the JCPDS Ref. Code 15 -0780 [22]. The sharp and intense nature of the diffraction peaks shows the high-quality polycrystalline nature of the prepared samples. It can be seen that the most intense (110) peak suffers a progressive shift towards higher diffraction angle with increase in Fe doping concentration (BF1 to BF7) in the $BaSnO_3$ lattice (Fig.1(b)). The slight shift in the peak position with increase in doping concentration Fe may be due to the difference in ionic radius of the host (Sn^{4+}) ion and dopant (Fe^{3+}) ion. The ionic radius of Sn^{4+} ion (0.69 Å) is larger than that of Fe^{3+} (0.55Å) ion with low-spin state or Fe $^{3+}$(0.645 Å) ion with high-spin state and can result in the distortion of host lattice [28]. Further, the presence of any additional peaks correspond to secondary phases are not visible in the XRD patterns and it gives an evidence for the partial substitution of Fe ions in the host lattice. The peak broadening and decrease in crystallite size with doping concentration also confirms that the dopant Fe ion involves in the growth mechanism of the synthesized compounds. The Rietveld analysis of XRD was done to understand the changes in structural parameters with Fe doping. The refinement of powder XRD patterns of $BaSn_{1-x}Fe_xO_3$ samples were carried out with the GSAS II software [29]. The background was fitted using shifted Chebyschev function and the peak profile parameters were refined using pseudo-Voigt functions.

The fitting can be judged by using R_p, R_{wp}, R_{exp} and χ^2 parameters where R_{wp} is the index that gives the idea of converging nature of refinement, R_{exp} is the expected statistical value for R_{wp}, R_p is related to the crystalline structure and $\chi^2=R_{wp}/R_{exp}$. A good fit corresponds to $\chi^2\sim1$ and $R_{wp}<5\%$. The Rietveld analysis of the pure and Fe doped $BaSnO_3$ samples are shown in Fig.2. The structural parameters obtained from the fit are given in Table.1. From the refined values, we can see that the lattice parameter of $BaSn_{1-x}Fe_xO_3$ shows a decrease with substitution of Fe ions when x changes from 0 to 0.07. This clearly indicates that the lattice constant shrinks with increase concentration of Fe and are caused by the difference in ionic radii of Sn and Fe ions. The average crystallite size in the prepared samples is calculated using Scherer formulae given as

$$D_{hkl} = \frac{k\lambda}{\beta_{hkl}\cos\theta_{hkl}} \quad (1)$$

where k is a constant, λ is the wavelength of the X-ray, β_{hkl} is the full width at half maximum (FWHM) and θ_{hkl} is the diffraction angle. The lattice parameter is found to be decrease with an increase in Fe doping concentration and their values for different samples are shown in Table1. The slight shift in the 2θ angle of doped Fe samples towards the higher 2θ region with respect to that of the pure sample produces a decrease in the value of lattice parameter. The variation in the intensity of the XRD peak and average crystallite size of the doped samples supports the Fe incorporation of the prepared samples. The variations in the lattice parameter and bond length can be due to the difference in the ionic radius of the exchanged cations and defects caused by the dopants [31,32].

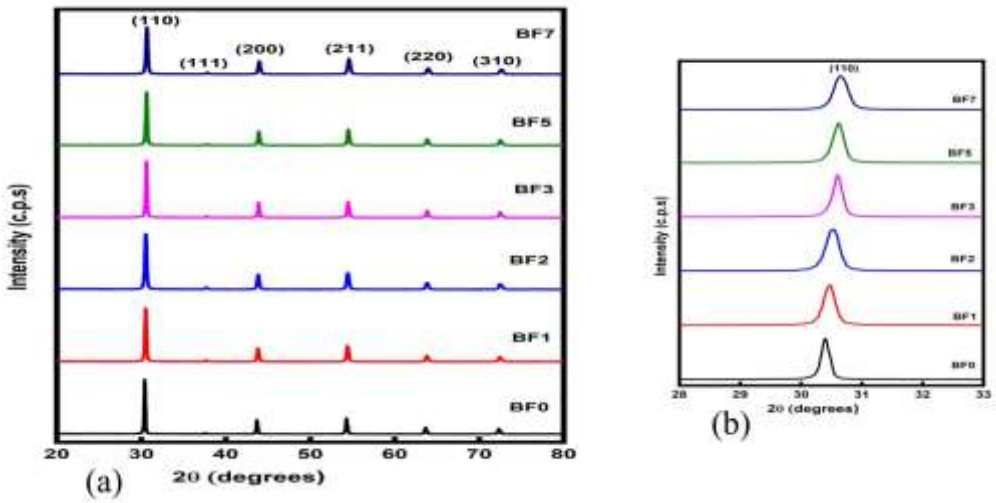

Fig. 1 (a) XRD patterns of the $BaSn_{1-x}Fe_xO_3$ (x=0.00, 0.01, 0.02, 0.03, 0.05 and 0.07) samples **(b)** The shift of (110) peak as a function Fe doping concentration of the $BaSn_{1-x}Fe_xO_3$ samples

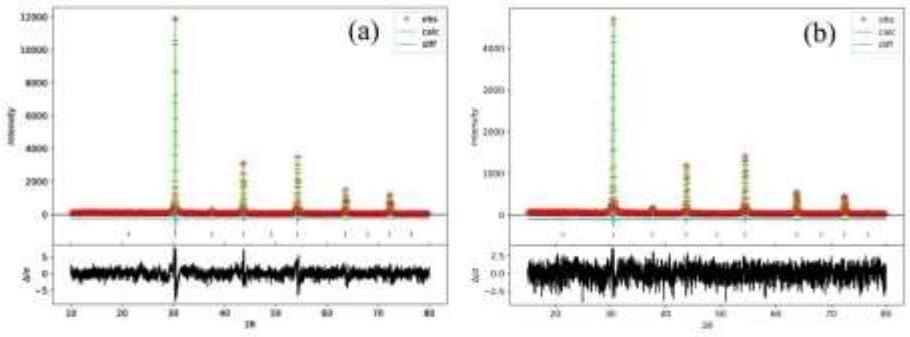

Fig. 2. Rietveld refinement of pure and Fe doped $BaSnO_3$ samples

Doping of an element can cause lattice deformation and introduce strain in the lattice of the compound. Williamson and Hall method can be used for finding the crystallite size and strain caused by the dopants in the host lattice [33]. Williamson and Hall relation is given by

$$\beta_{hkl}cos\theta_{hkl} = \frac{k\lambda}{D'} + 2\eta\sin\theta_{hkl} \qquad \text{----- (2)}$$

where D' is the average crystallite size in nanometers, η is the microstrain.The slope of the Williamson–Hall (W-H) plot gives the strain and from the Y intercept, we can calculate the average crystallite size. From Fig.3 it is found that all the prepared samples have tensile strain and this can be due to the incorporation of the dopant ions in the host lattice. The lattice strain of the pure and the Fe doped $BaSnO_3$ calculated from the W-H plot is shown in Table 1. The value of the strain in the compounds is found to be decreased with an increase in dopant concentration. Thus the XRD analysis suggests the incorporation of dopant ion in the host Ba-Sn-O lattice.

Table 1.Rietveld refined structural parameters of pure and Fe doped $BaSnO_3$ samples

Parameters	BF0	BF1	BF2	BF3	BF5	BF7
a=b=c (Å)	4.1161(2)	4.1134 (1)	4.1133(3)	4.1132 (3)	4.1101(3)	4.1063 (4)
α=β=γ	90	90	90	90	90	90
volume	69.736	69.592	69.601	69.601	69.432	69.239
density	7.239	7.239	7.223	7.2083	7.195	7.185
R_{exp}	0.0852	0.130	0.117	0.118	0.1126	0.111
R_{wp}	0.095	0.116	0.1039	0.0779	0.119	0.127
(χ^2)	1.240	1.135	1.186	1.054	1.072	1.144
Bond length Sn-O	2.0582	2.05663	2.05672	2.05672	2.0550	2.0531
Crystallite size (nm)	45	38	34	30	35	31
Lattice strain	0.0050(14)	0.0042(23)	0.0039(17)	0.0038(26)	0.0037(63)	0.00242(95)

Table 2 Atomic coordinates and Uiso parameters of pure and Fe-doped $BaSnO_3$ compounds

	Atom site	x	y	z	Uiso
BF0	Ba	0.5000	0.5000	0.5000	0.012(11)
	Sn	0	0	0	0.009(11)
	O	0	0	0.5	0.009(12)
BF3	Ba	0.5000	0.5000	0.5000	0.019(4)
	Sn	0	0	0	-0.011(4)
	Fe	0	0	0	-0.011
	O	0	0	0.5	-0.000(10)

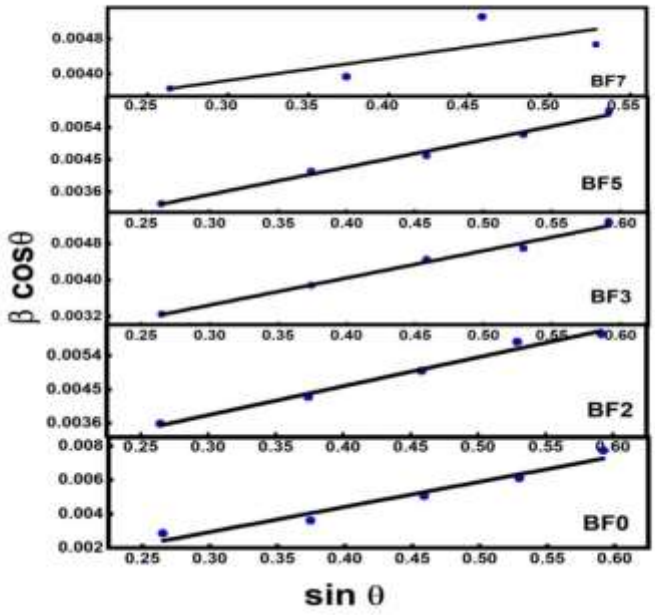

Fig. 3 Williamson–Hall plot of pure $BaSnO_3$ and Fe doped $BaSnO_3$ samples

3.2 Raman analysis

Micro Raman analysis is a sensitive tool to determine the structural changes in pure and doped samples. The partial substitution or replacement of atoms A or B cations in an ideal perovskite ABO_3 (cubic) lowers the symmetry of the structure and this can be clearly evidenced from the Raman spectroscopy [34]. Fig.4 shows the micro Raman spectra of $BaSnO_3$ and Fe doped $BaSnO_3$ samples. In general, the $BaSnO_3$ having an ideal cubic structure with space group Pm3m did not show first-order Raman scattering because of its centrosymmetric crystal structure [27]. The Raman bands observed in Raman spectra of these samples can be due to the presence of defects or dopants. The undoped sample exhibit the Raman modes at 140, 193,332, 410, 561, 712, 835 and 1056 cm^{-1}. These modes are due to the six fundamental vibrations of SnO_6 octahedron which has O_h symmetry, in the distorted perovskite structure. The bands found at 561, 190 and 140 cm^{-1} are due to Raman active *v*2Eg, *v*4F1u and *v*5F2g modes respectively [35]. The difference in the spectral behavior of the pure $BaSnO_3$ and Fe doped $BaSnO_3$samplescan be

clearly evidenced from the Raman spectra. The bands at 561, 657, 712 cm^{-1} are attributed to the Sn-O vibration modes. The observed band shift and the enhanced broadening observed for the Sn-O bond can be attributed to the distortion of SnO_6 octahedron due to the Fe incorporation of Fe in the host lattice. The band observed around 650 cm^{-1} shows a systematic shift towards the lower wavenumbers as the Fe doping concentration increases. The medium intense band observed at 561 cm^{-1} in the Raman spectrum of pure $BaSnO_3$ sample can be due to the second order Raman mode and its intensity decreases and appears as a shoulder band in the Raman spectra of Fe doped samples. Also the intensity of the Raman band around 410 cm^{-1} decreases in Fe doped samples. The band around 835 cm^{-1} possibly due to the defect induced oxygen vacancies and shows a systematic band shift towards higher wave numbers as Fe doping concentration increases. The intensity and broadening of the band around 835 cm^{-1} gets enhanced as Fe doping concentration increases. The band 1056 cm^{-1} appears in the pure $BaSnO_3$ and Fe doped $BaSnO_3$ with low Fe doping concentration. In samples with higher doping concentration, the intensity gets suppressed and appears as broad band. The peak obtained at 220, 330 cm^{-1} in the pure and Fe doped compound correspond to the defects or oxygen vacancies in $BaSnO_3$ [35].

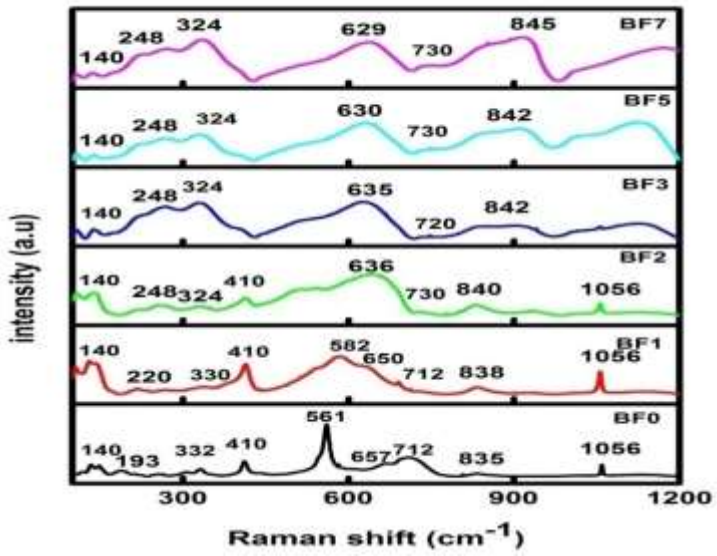

Fig. 4 Micro-Raman spectra of pure $BaSnO_3$ and Fe doped $BaSnO_3$ samples

3.3 FTIR Analysis

The FTIR spectra of the pure $BaSnO_3$ and Fe doped $BaSnO_3$samples measured in the range 4000-400 cm^{-1} are shown in Fig.5. The IR spectra below 1000 cm^{-1} correspond to Sn-O bonds or the deformation modes of Sn-O bonds in SnO_6 octahedral. The peak at 624 cm^{-1} may be assigned to asymmetric stretching of Sn–O bonds [36] and the peak at 490 cm^{-1} may be due to Sn-O vibration at the octahedral sites. The peak position at 852 and 1476 cm^{-1}shows C–O stretching vibrations due to the moisture absorbed from atmospheres by the material and the asymmetric stretching vibration of Sn–OH bonds respectively [37].The slight variation in the position of the Sn-O band may be due to the incorporation of Fe ions in the doped samples.

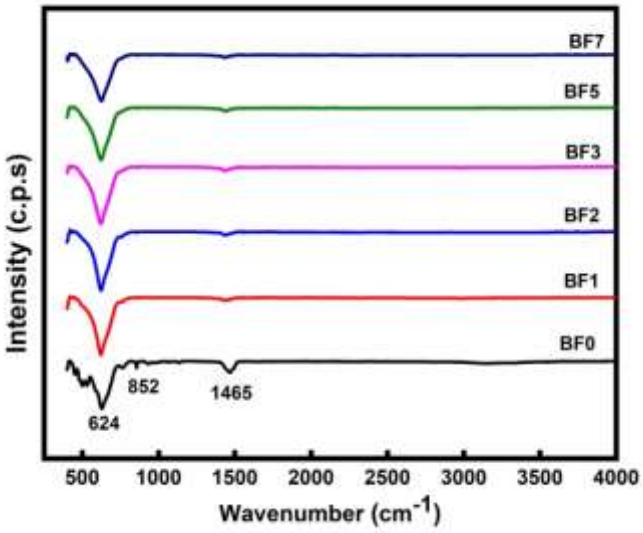

Fig. 5.FTIR spectra of pure $BaSnO_3$ and Fe doped $BaSnO_3$ samples

3.4 Morphological Analysis

Field emission scanning electron microscopy (FESEM) was used for analyzing the surface morphology of the prepared compounds. Fig. 6 shows the FESEM images of pure $BaSnO_3$ and Fe doped $BaSnO_3$ compounds. From the images, it is observed that the pure $BaSnO_3$ particles (BF0) were of cuboidal shape with irregular size having a high degree of agglomeration. Also, from the FESEM images, it is observed that on doping Fe with different concentrations the shape of these particles changed into nanorods. This may be due to the involvement of Fe ions in the

growth mechanism and will alter the surface morphology. The size and shape of compounds depend on nucleation and grain growth processes. In general, the particles with higher surface energies tend to grow faster than those with lower surface energies which results in non-uniform growth and the particles tend to minimize their surface free energy by growing into larger particles [38]. Thus the poly-dispersed particles combine together to form hexagonal rod like structure [36]. The equilibrium shape of a crystal corresponds to the minimization of the total surface energy, which varies with the orientation of the crystal [39]. The formation of rod-shaped particles is more pronounced for 3 mol% Fe dopant concentration. Fig.7 shows the EDS mapping and spectra of Fe doped $BaSnO_3$ (BF3) sample and it confirms the presence of the constituent elements in the prepared compounds. The TEM images (Fig.8(a),8(c)) and the SAED pattern (Fig. 8(b), 8(d)) of pure and Fe doped samples shown respectively support the FESEM analysis. The formation of a rod-shaped particle of the Fe doped sample can be confirmed from the TEM analysis.

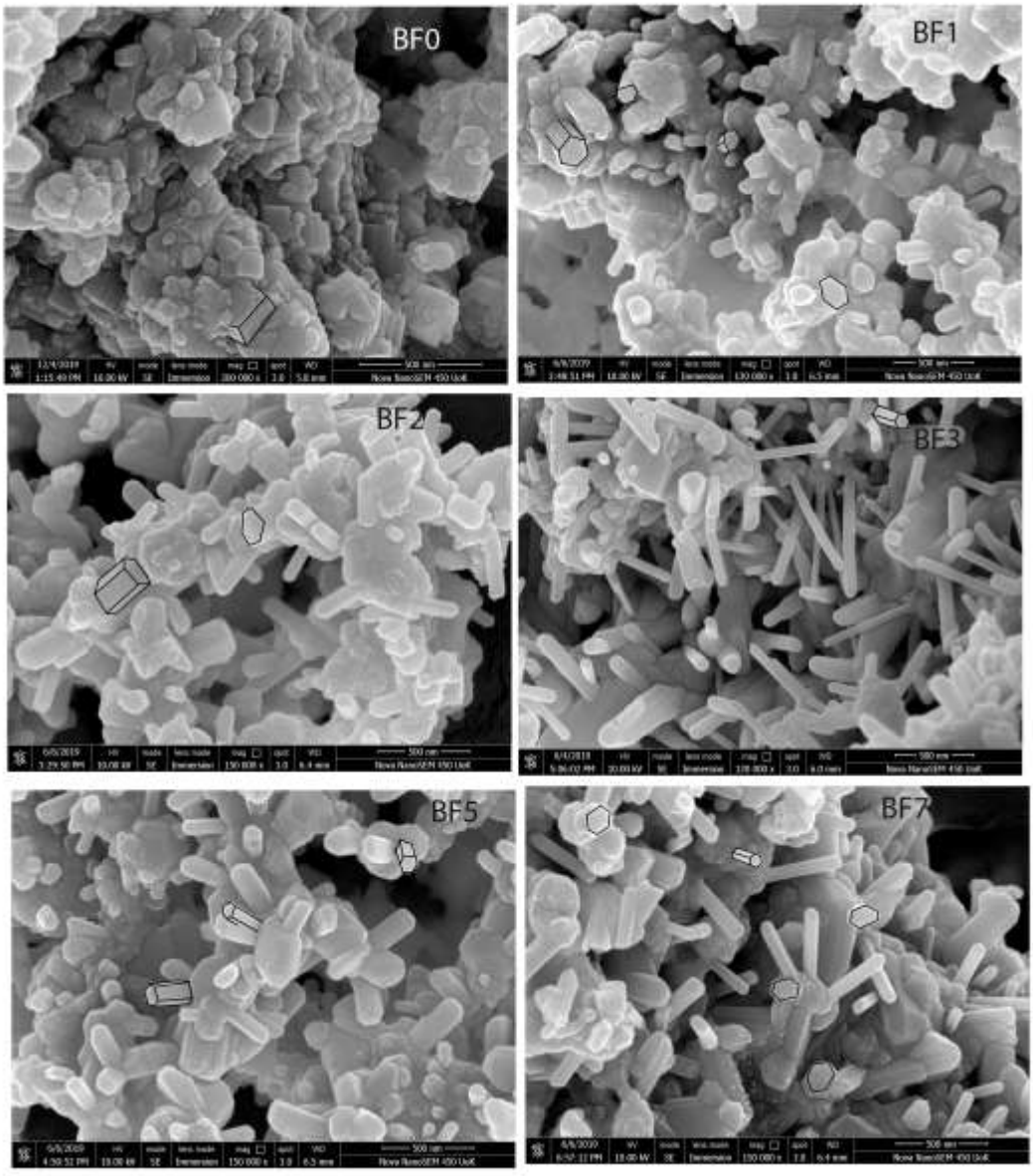

Fig.6. FESEM of pure and Fe-doped $BaSnO_3$ samples

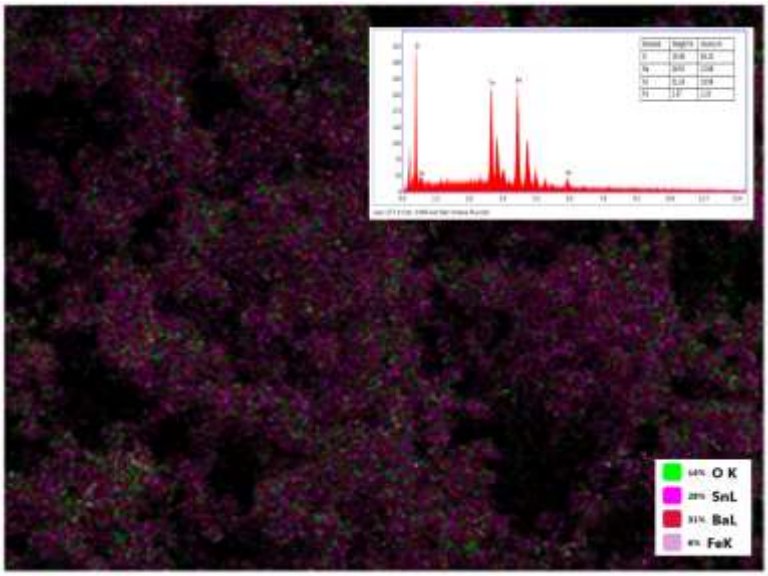

Fig.7.EDS mapping and spectra of BF3 sample

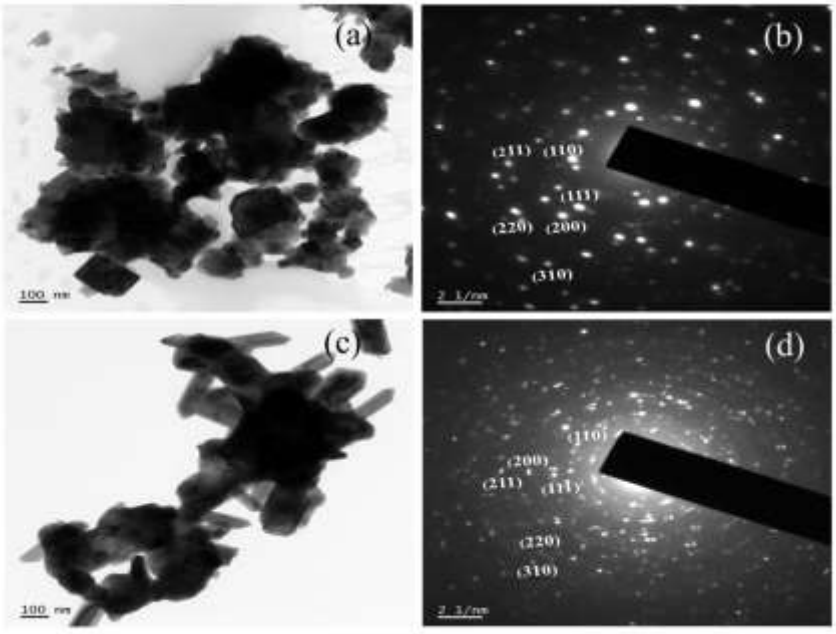

Fig. 8 (a), (c) TEM images, **(b)** and **(d)** SAED pattern of pure and Fe doped $BaSnO_3$ (BF3) samples

3.5. XPS Analysis

The oxidation state and surface chemical composition of elements present in the prepared pure $BaSnO_3$ and Fe doped $BaSnO_3$ compound were analyzed by X-ray photoemission spectroscopy (XPS). The XPS survey spectrum of pure $BaSnO_3$ compound is shown in Fig. 9 (a) and it shows peaks correspond to elements Ba, Sn, O and C. The C1s peak can be due to the presence of contamination on the surface of the synthesized compound. The fitted and core-level XPS spectra of Ba with doublet peaks having binding energy 779.6 eV and 794.9 eV corresponding to Ba $3d_{5/2}$ and Ba $3d_{3/2}$ states respectively are shown in Fig. 9(b). The separation between the peak Ba $3d_{5/2}$ and Ba $3d_{3/2}$ states representing the binding energy 15.3 eV confirms that the valence state of barium is in Ba^{2+} state [40, 41]. Fig.9(c) shows the core level splitting of the Sn3*d* spectrum having the spin-orbital splitting, for the Sn (3d) state with $3d_{5/2}$ and $3d_{3/2}$ states having doublet peaks with binding energy values 485.4 eV and 493.8 eV respectively with a peak separation of 8.4 eV. The separation of Sn spin-orbit doublet corresponds to the Sn^{4+} state [42, 43]. The deconvoluted and core level O1s spectrum of the pure sample is shown in Fig. 9(d). The deconvoluted O1s have three peaks corresponding to binding energies 528.78, 530.09 and 530.64 eV respectively. The lower binding energy corresponds to the lattice oxygen species (O^{2-}) [44]. The intermediate and the higher binding energy values correspond to the adsorption oxygen species and the oxygen vacancy present in the compound respectively [44].

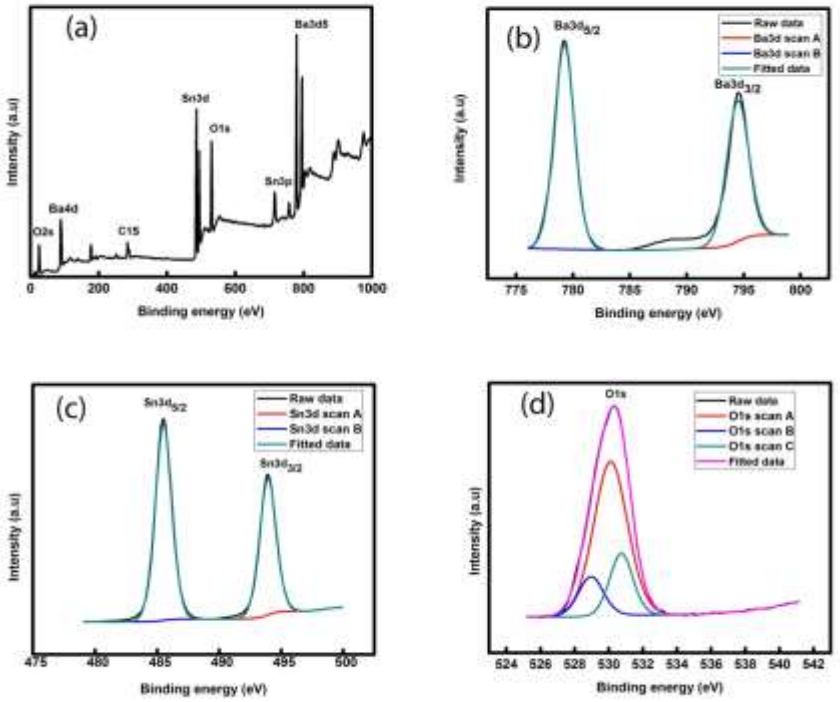

Fig. 9. XPS analysis of pure $BaSnO_3$ powder sample **(a).** XPS survey spectrum **(b).** core level splitting of peaks of Ba **(c).** the core level splitting of peaks of Sn and **(d).** the core level splitting of peaks of O.

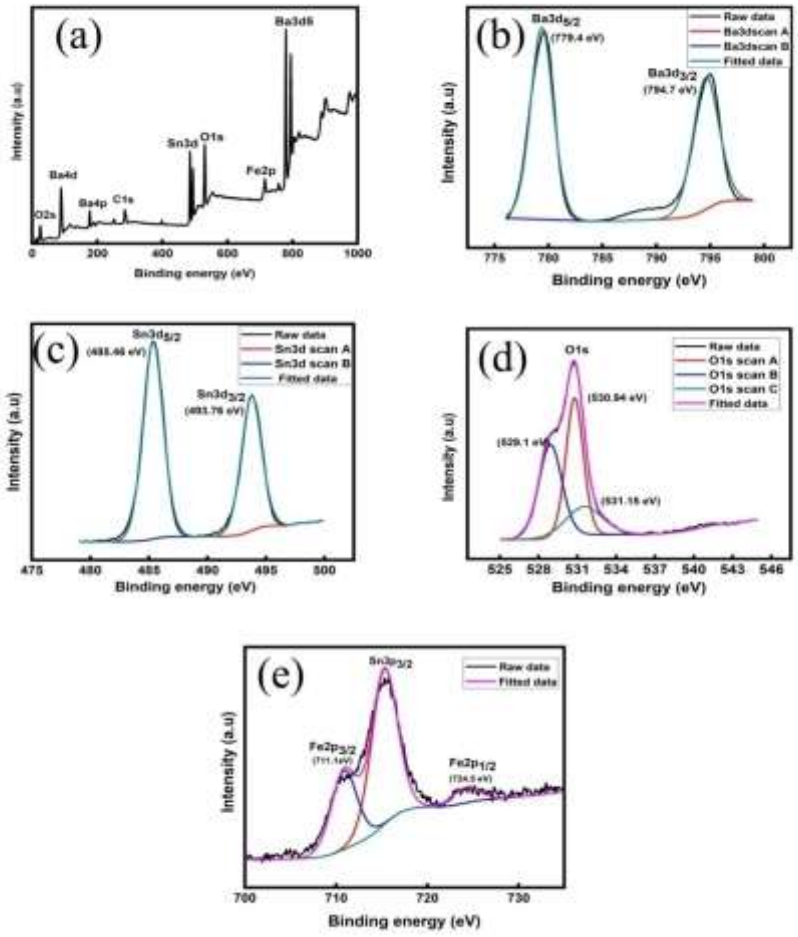

Fig. 10. XPS analysis of Fe doped $BaSnO_3$ (BF3) powder **(a).** XPS survey spectrum **(b).** core level splitting of peaks of Ba **(c).** core level splitting of peaks of Sn **(c)**. core level splitting of peaks of Oand **(d).**core level splitting of peaks of Fe.

The XPS survey spectrum of 3 mol% Fe doped $BaSnO_3$ compound are shown in Fig. 10(a) and shows the peak corresponding to constituent elements Ba, Sn, O and Fe. The Fe doped $BaSnO_3$ has the spin-orbit doublet splitting of element Ba with Ba $3d_{5/2}$ and Ba $3d_{3/2}$ states (Fig. 10(b)) with the binding energy value 779.4 and 794.7 eV and peak separation of 15.3eV.This binding energy value corresponds to Ba^{2+} state [40]. The spin-orbit doublet of Sn $3d_{3/2}$ and Sn $3d_{5/2}$ states (Fig.10(c)) with binding energy values at 485.46 eV and 493.76 eV presents a binding energy peak separation of 8.3 eV [42]. The XPS spectrum of O1*s* peak can be fitted and deconvoluted

into three peaks centered at 529.1 eV, 530.94 eV and 531.15 eV (Fig.10 (d)). The lowest binding energy (529.16 eV) peak is associated with lattice oxygen. The peak corresponding to binding energy at 530.94 eV corresponds to the adsorption oxygen species (O_2^{2-}) and the peak corresponding to the binding energy 531.15 eV represents the oxygen vacancy in the compound [44,45]. The binding energy shift of the lattice oxygen and the shoulder peak indicates that the Fe ions indeed influence the optical properties of the $BaSnO_3$ compound and it is also confirmed from the UV-Visible analysis with Fe dopant concentration. The fitted and core-level XPS spectrum of Fe doped BF3 sample is shown in Fig. 10(e). The observed binding energy of Fe in 711.1 and 724.5 eV correspond well with the characteristics of Fe^{3+} and confirms Fe in 3+ oxidation state (Fig.4. 10 (e))[46]. The peak around 715.4eV corresponds to theSn $3p_{3/2}$ state of the Sn element.

3.7 UV–Visible analysis

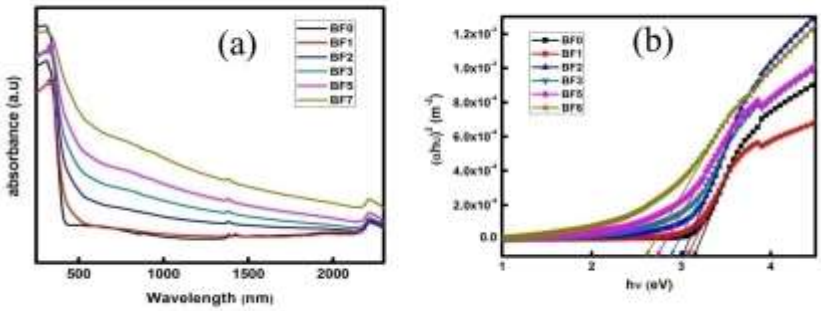

Fig.11.(a) Absorption spectra and **(b)** Tauc plot of pure and Fe-doped $BaSnO_3$ samples

Fig.11 (a) shows the absorbance spectra of the pure and Fe doped $BaSnO_3$samples in the wavelength region 250-2500 nm. The shift of optical absorption to the longer wavelength region due to Fe doping can be clearly evidenced from the absorbance spectra and it is due to the possible electronic transitions between dopant ions and host ions. The absorption peak of the samples can be due to the charge transfer between the oxygen and metal in SnO_6 octahedral

groups. The optical band gap (E_g) values of pure and doped samples were determined using the Tauc plot equation [40] given as

$$\alpha(h\nu) = A(h\nu - E_g)^n \quad (3)$$

where α is the absorption coefficient, h is the Planck's constant, ν is the frequency of radiation and A is the band edge sharpness. For all the samples the straight line Tauc plot is obtained for the case of exponent n = ½ which corresponds to direct allowed transition [47]. By extrapolating the plot between $(\alpha h\nu)^2$ versus hν, the bandgap energy of pure and doped $BaSnO_3$ samples can be found out which is shown in Fig.11 (b). The bandgap energy value for pure $BaSnO_3$ was found to be 3.15 eV which is in agreement with the previously reported value [22]. It is found that the bandgap energy value decreases systematically with increase in Fe doping concentration. There will be a formation of new intermediate energy levels due to the dopant atoms in the host lattice. Similar behavior of redshift in the bandgap of the Cr and Mn doped $BaSnO_3$ nanostructures is reported [48, 49]. Thus the optical absorption spectrum clearly gives an evidence for the interaction between the host $BaSnO_3$ lattice and the doped Fe atoms.

3.8 Nonlinear Optical Properties

The nonlinear optical properties of pure and Fe doped $BaSnO_3$samples were measured by the open aperture Z-scan technique. The samples were excited using a Q-switched Nd:YAG laser at the second harmonic emission at wavelength of 532 nm. In this experiment, the laser beam is focused using a convex lens. The sample is placed at different positions with respect to the focal point, and the corresponding optical transmissions are measured. The position-transmission curve thus obtained is called the open aperture Z-scan curve, from which the nonlinear absorption coefficient of the sample can be calculated. The open aperture Z-scan transmittance of the prepared $BaSn_{1-x}Fe_xO_3$ (x =0, 0.01, 0.03, 0.05 and 0.07) samples are shown in Fig.12(a). The circles represent the experimental data and the solid lines represent theoretical fits to the data. The valley shape of the open aperture Z-scan curves indicates strong reverse saturable absorption (RSA) taking place in the samples.

The nonlinear absorption coefficient can be found out by

$$\alpha(I) = \frac{\alpha_0}{\left(1+\frac{I}{Is}\right)} + \beta I \quad (4)$$

Where α_0 is the linear absorption coefficient at the excitation wavelength, 'I' is the input laser intensity, I_s is the saturation intensity and β is the third order RSA coefficient. The corresponding differential equation describing the nonlinear propagation of light through the sample is given by

$$\frac{dI}{dz'} = -\left[\frac{\alpha_0}{\left(1+\frac{I}{Is}\right)} + \beta I\right] I \qquad (5)$$

which can be fitted numerically to the measured data to find I_s and β. Here, z' is the propagation distance within the sample [49]. The normalized transmittance plotted as a function of input intensity (Fig.4.12(b)) reveals the RSA behavior of the samples. Values of β and I_s, calculated from the numerical best fits to the experimental data, are given in Table 3. It is interesting to note that as the Fe doping concentration is increased the reverse saturable absorption coefficient increases systematically. The increase of β values with Fe dopant concentration may be due to the decrease in the variation of bandgap energy of the samples. The obtained β values are fairly high, of the order of 10^{-11} mW^{-1}.Also it is to be noted that as the Fe doping concentration is increased the value of saturation intensity decreases. The highest value of β ($1.1x10^{-10}$ m/W) and the lowest value of saturation intensity ($0.3x\ 10^{13} W/m^2$) is obtained for BF7 samples. The strong RSA nature of these samples makes them ideal candidates for optical power limiting applications. A similar trend of increase of β values and decrease of I_s value with increase in doping concentration is obtained for Mn doped samples [49].

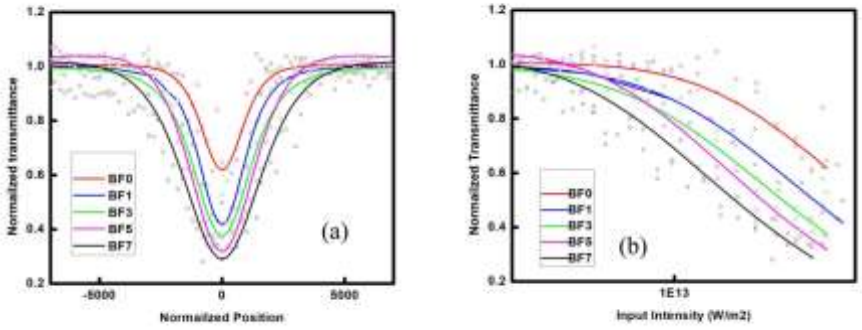

Fig.12.(a) Open-aperture Z-scan curves measured for pure and Fe doped $BaSnO_3$ samples. (**b)** The normalized transmittance calculated as a function of input intensity. Symbols are data points while solid curves are numerical fits calculated using equation 5.

Table 3. Nonlinear optical parameters of the prepared pure and Fe doped $BaSnO_3$ samples.

Sample code	Is (W/m^2)	Nonlinear absorption coefficient (m/W)
BF0	1.4×10^{13}	0.3×10^{-10}
BF1	1.0×10^{13}	0.48×10^{-10}
BF3	0.8×10^{13}	0.66×10^{-10}
BF5	0.4×10^{13}	0.86×10^{-10}
BF7	0.3×10^{13}	1.1×10^{-10}

3.6 Photoluminescence analysis

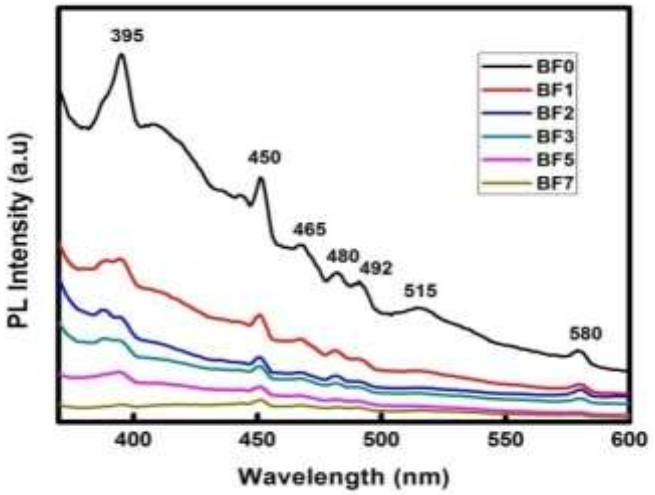

Fig.13. PL spectra of pure and Fe doped $BaSnO_3$ powder samples with different Fe dopant concentration

PL is a sensitive technique used for the analysis of defect states and the disorder cluster parameters present in the prepared samples. Fig. 13 shows the room temperature PL spectra of pure and Fe doped $BaSnO_3$ compounds when excited with a radiation of wavelength of 350 nm. Doping of iron creates defects in $BaSnO_3$ system. Pure and Fe doped $BaSnO_3$ compounds exhibit emission at 395nm (3.1eV) which corresponds to the band edge. UV-Visible spectra show a systematic decrease of band gap energy with increase in Fe doping concentration. In the PL spectra also these peaks show a red shift. The blue-green emission peak with 450 nm and 465 nm can be attributed to the transitions within the defect centers, such as oxygen vacancies in the compounds [47, 48]. An emission peak at 480nm (2.57eV) is attributed to the transitions of Sn $3P^0_1$ -$1D_2$. The peak at 492 nm (2.52eV) can be ascribed to Ba $3P_0^2$ - $3D_3$ transitions. The less intense peak observed near 515 nm is due to Ba $3P^0$-$3D_1$ transitions [48].

3.9 Magnetization studies

The field-dependent magnetization of pure and Fe-doped $BaSnO_3$ compounds is shown in Fig.14. As reported, undoped sample (BF0) shows diamagnetic nature [29] and with an increase in Fe doping concentration there arises a positive value of magnetic moments. The magnetic moment monotonically varies with Fe concentration. The inset of Fig. 14 shows the well-defined hysteresis loop of Fe doped $BaSnO_3$ compounds with coercivity ranges from 73 to 235 Oe which indicate the existence of ferromagnetic domains in the Fe doped samples. The possible reasons for the FM ordering at room temperature has been explained by various authors [29,40]. It is reported that the spin of the electron trapped in the oxygen vacancy interacts with each spin of Fe ions within its orbital and results in Fe-Vo-Fe configuration which leads to ferromagnetic order between the two Fe ions. Also, the observed magnetic moments can be due to F-centre exchange (FCE) mechanism of Fe-V_0-Fe in which direct ferromagnetic coupling of metal ions takes place through an oxygen vacancy [50]. Pratiba et al., reported the origin of ferromagnetic behavior in Fe doped $BaSnO_3$ is through electrons trapped at defects such as the oxygen vacancies (F center) form a bound magnetic polaron [51]. Coey et al., [52] reported the bound magnetic polaron (BMP) model for the observed ferromagnetism in Fe doped $CaSnO_3$ and for magnetic ordering in insulating systems. When the concentration of Fe increases, oxygen vacancies are expected to arise near Fe sites and *d* electrons of Fe are supposed to interact through FCE [49, 53]. Thus, Fe spins may align parallel along the field which leads to ferromagnetic coupling and increased magnetization behavior in the prepared compounds.

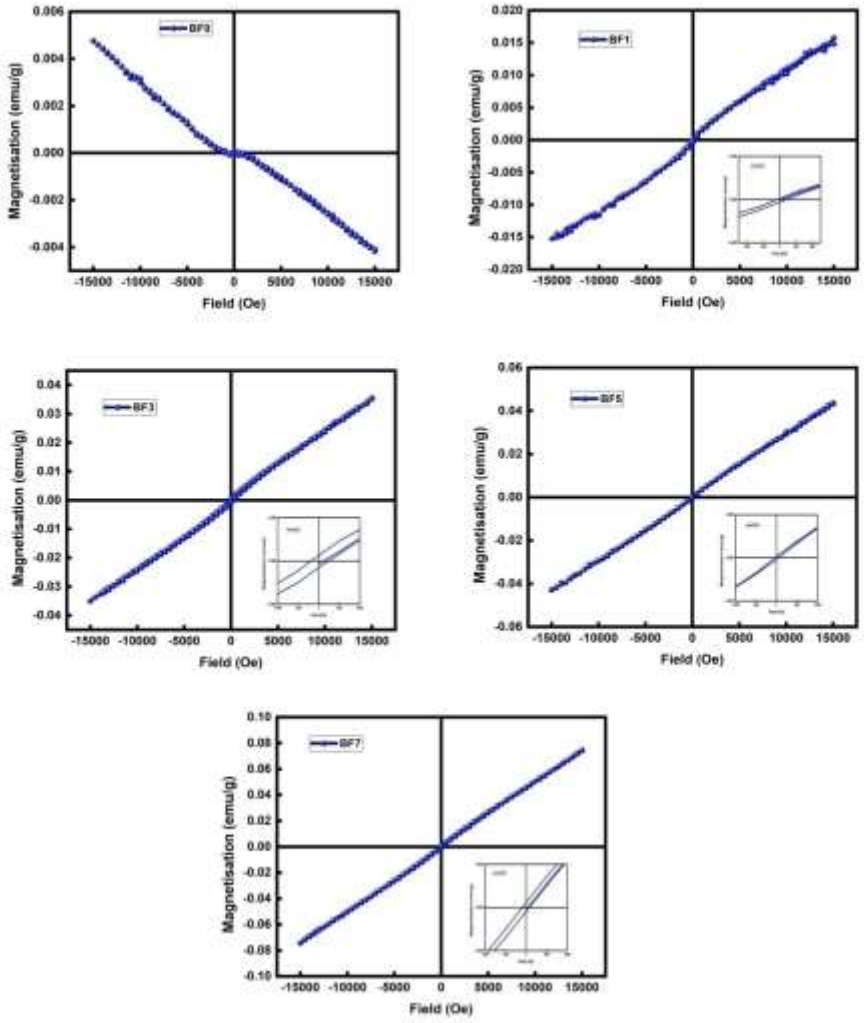

Fig.14. *M-H* curve of pure and Fe-doped $BaSnO_3$ at *T*= 300K

3.10 EPR Studies

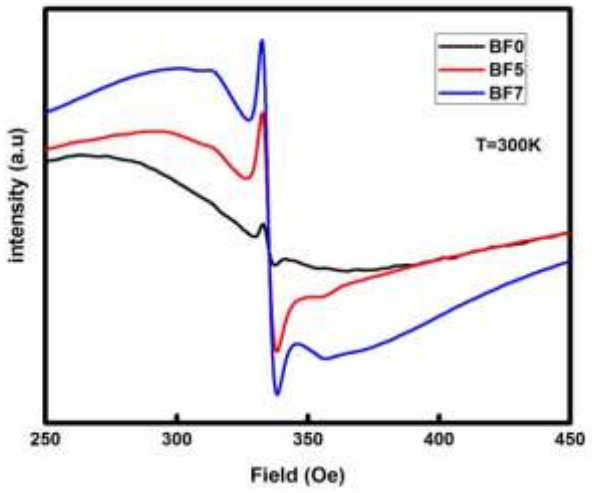

Fig.15. EPR spectra of pure and Mn-doped $BaSnO_3$ samples

Electron Paramagnetic Resonance (EPR) studies were used to study the magnetic microstructure and the presence of unpaired electrons. Fig.15 shows the EPR spectra of pure and Fe doped $BaSnO_3$ samples recorded at room temperature. From the figure, it is observed that pure and all Fe doped $BaSnO_3$ compounds exhibits resonance signals. It is known that the pure $BaSnO_3$ compound is found to be EPR inactive due to the absence of unpaired electrons [54]. But in the present work, EPR is active for pure $BaSnO_3$ compound which reveal the presence of F-centers created by the electrons trapped at (oxygen) anion vacancies [55]. Since the samples have prepared by high temperature solid-state synthesis route, that can lead to the formation oxygen vacancies. The oxygen vacancies act as double electron donors having charge carriers and the spins can polarize through exchange interactions. The sharp resonance signal that appeared with g ~ 2.0 may be attributed to the oxygen vacancy electron center [36, 56]. In the case of Fe-doped samples, the intensity of F-center signal is higher compared with that of pure sample and the g value is found to be ~1.99. It is reported that the g value of isolated Fe^{3+}ions is very close to that of a free electron [57]. Hence, the observed signals at ~ 338 Oe indicate the presence of isolated Fe^{3+} ions. It is also noted that there appears broad and less intensity signals at higher field region and it can be due to the ferromagnetic coupling of Fe^{3+} pairs [22]. The broad ferromagnetic

resonance signal with *g* value of 1.95 is caused by the exchange interactions between Fe^{3+} ions [58]. The EPR studies reveal the possible ferromagnetic ordering of Fe doped samples.

3.11 Dielectric Analysis

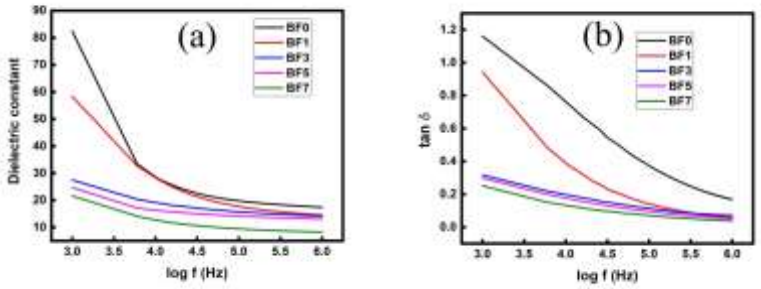

Fig. 16 Variation of (a) dielectric constant (b) loss tangent for pure and Fe doped $BaSnO_3$

Dielectric properties of a material such as dielectric constant, dielectric loss will depend on different parameters such as frequency of the applied field, temperature, structure, particle size etc. and is an important property for designing optoelectronic devices. Figure 16 shows the dielectric properties of pure and Fe doped $BaSnO_3$in a wide range of frequencies taken at room temperature. The dielectric constant (Fig.16 (a)) is found to be decreasing with increasing frequency for all the pure and Fe doped samples. The dielectric constant is maximum for low frequency and is minimum for high frequency and this behavior can be due to Maxwell-Wagner model polarization [59] in which material is composed of conducting grains separated by poor conducting grain walls. At low frequency, grain boundary is more effective and at high frequency grains are effective. For higher frequency, due to accumulated charge carriers within the grain boundary, it cannot follow the applied field, which decreases the dielectric constant [60]. It is reported that the high values of dielectric constant at low frequencies can be due to oxygen vacancies, grain boundaries effect, interfacial dislocations, charged defects, and space charge polarization due to heterogeneous dielectric structure [61]. The decrease in dielectric constant with Fe doping may be due to the decrease in polarizability caused by the neutralization

of Fe ions with oxygen ions [62]. Fig. 16 (b) shows the variation of dielectric loss (tan δ) values of prepared pure and Fe doped $BaSnO_3$ as a function of frequency. The energy loss in the system with the applied field is represented by loss tangent (tanδ). From the Fig.16 (b), we can see that dielectric loss values decrease with the increase of frequency for pure and doped samples which may be due to the space charge polarization. The pure $BaSnO_3$ sample has maximum loss which decreases with Fe doping and has a gradual decrease in the higher frequency regime.

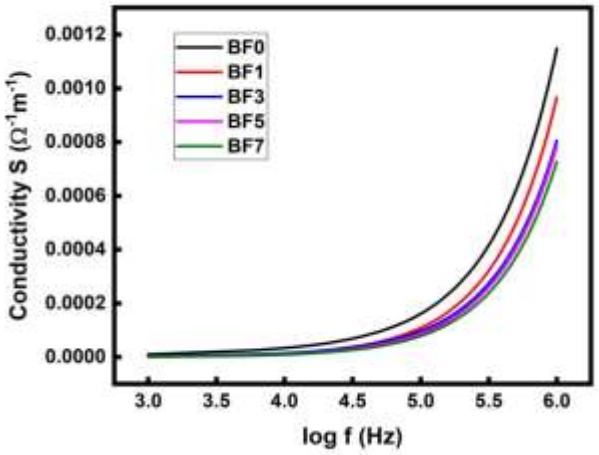

Fig.17. Variation in ac conductivity of pure and Fe doped $BaSnO_3$ with frequency

Fig. 17 shows the variation of conductivity with the frequency of pure and Fe doped $BaSnO_3$. The ac electrical conductivity of the synthesized pure and Fe compounds is calculated using the relation

$$\sigma (ac) = \varepsilon' \varepsilon_0 \omega \tan\delta \qquad \text{-----(6)}$$

where ε_0 and ε' are the permittivity of free space and material respectively and ω is the frequency of the applied field. The conductivity of all the samples is found to be increasing with the increase of frequency and this may be due to the hopping between the charge carriers. For a particular frequency, conductivity is found to decrease with the increase in Fe concentration. Similar behavior is reported in the case of Co-doped ZnO [63]. The reason behind this may be due to the increase in Fe concentration produces defect ions such as oxygen vacancies in the host system segregate at the grain boundaries. The grain boundary defect barrier leads to the blockage

to the flow of charge carriers and results in decreases in conductivity with Fe dopant concentration [64]. The Fe dopant in the host lattice ceases the hopping mechanism resulting in the decrease of electrical conductivity with an increase in Fe concentration. Also, the DC electrical resistivity of the Fe doped compounds is found to increase with doping concentration and is in the range of $10^7 \Omega$m.

4. Conclusion

Perovskite pure and Fe doped $BaSnO_3$ compounds were synthesized by the solid-state method. XRD patterns reveal that the pure and the doped samples have the polycrystalline cubic phase. Rietveld analysis gives information about the change in the lattice parameter and the Sn-O bond lengths of Fe doped samples. The structural identification of the prepared compounds was done by micro-Raman and FTIR spectra. The morphological behavior shows that there is a change in the shape of particles from cuboidal to rod shape. The elemental analysis of the prepared compounds was done by EDS and XPS analysis. The presence of oxygen vacancies was confirmed from the XPS and EPR analysis. The observed enhancement in the feeble magnetic moments with Fe doped $BaSnO_3$ compounds is beneficial in spintronic device applications. The nonlinear optical absorption exhibited by the synthesized compounds can be used for optical power limiting applications. The observed decrease in the dielectric loss with Fe doped samples has useful applications in optoelectronics and in high frequency devices.

References

1. Zhe Wang, Hanjong Paik, Zhen Chen, David A. Muller, Darrell G. Schlom, Epitaxial integration of high-mobility La-doped $BaSnO_3$ thin films with silicon, APL Mater. 7, 022520 (2019) doi: 10.1063/1.5054810
2. T. Ishihara, K. Kometani, M. Hashida, Y. Takita, J. Mixed Oxide Capacitor of $BaTiO_3$–PbO as a New Type CO_2 Gas Sensor, Am. Chem. Soc. 75, 613 (1992)
3. J. Cerda, J. Arbiol, R. Diaz, G Dezanneau, J. R. Morante,Synthesis of perovskite-type $BaSnO_3$ particles obtained by a new simple wet chemical route based on a Sol–gel process, Mater. Lett. 56 (2002)131-136
4. A.M. Azad, L.L.W. Shyan, P.T. Yen, N.C. Hon,. Microstructural evolution in $MSnO_3$ ceramics derived via self-heat-sustained (SHS) reaction technique Ceram. Int. 26, (2000), 685
5. Qinzhuang Liu , Jianjun Liu, Bing Li, Hong Li, Guangping Zhu, Kai Dai, Zhongliang Liu, Peng Zhang, *and* Jianming Dai, Composition dependent metal-semiconductor

transition in transparent and conductive La-doped $BaSnO_3$ epitaxial films Appl. Phys. Lett. 101, 241901 (2012); https://doi.org/10.1063/1.4770299

6. U. Lumpe, J. Gerblinger, H. Meixner, Nitrogen oxide sensors based on thin films of $BaSnO_3$, Sens. Actuators B 26–27, 97 (1995)
7. M.G. Smith, J.B. Goodenough, A. Manthiram, R.D. Taylor, W. Peng, C.W. Kimbal, J. Tin and antimony valence states in $BaSn_{0.85}Sb_{0.15}O_{3-\delta}$, Solid State Chem. 98 (1992) 181.
8. P.H. Borse, U.A. Joshi, S. M. Ji, J. S. Jang, J. S. Lee. Band gap tuning of lead-substituted $BaSnO_3$ for visible light photocatalysis, Appl. Phys. Lett. 90, (2007) 03410
9. Bernhard Ostrick , Maximilian Fleischer, Uwe Lampe, Hans Meixner, Preparation of stoichiometric barium stannate thin films: Hall measurements and gas sensitivities Sensors and Actuators B 44 (1997) 601–606
10. A.Marikutsa, M.Rumyantseva, A.Baranchikov, Alexander Gaskov, Nanocrystalline $BaSnO_3$ as an Alternative Gas Sensor Material: Surface Reactivity and High Sensitivity to SO_2 Materials, 8, (2015), 6437-6454 276
11. K. Balamurugan, N. H. Kumar, B. Ramachandran, M.S. Ramachandra Rao, J. A. Chelvane,P.N. Santhosh, Magnetic and optical properties of Mn-doped $BaSnO_3$ Solid State Communications 149 (2009) 884-887
12. A. L. M. de Oliveira, V.Bouquet, V.Dorcet, S. Ollivier, S. Députier, A. Gouveia de Souza, M. SiuLi, E. Longo, I. Távora Weber, I.M.Garcia, Evolution of the structural and microstructural characteristics of $SrSn_{1-x}Ti_xO_3$ thin films under the influence of the composition, the substrate and the deposition method dos Santos, M.Guilloux-Viry, Surf.Coat.Technol.313 (2017) 361-373.doi:10. 1016/j.surfcoat.2017.01.082
13. S.A. Wolf, Spintronics: A Spin-Based Electronics Vision for the Future Science 294, 1488–1494 (2001)
14. Upadhyay S, Parkash O and Kumar D, Synthesis, structure and electrical behaviour of lanthanum-doped barium stannate, J. Phys. D: Appl. Phys. (2004) 37 1483
15. H. J. Kim, U. Kim, T. H. Kim, J. Kim, H. M. Kim, B. G. Jeon, W. J. Lee, H. S. Mun, K. T. Hong, J. Yu,Physical properties of transparent perovskite oxides (Ba,La)SnO3 with high electrical mobility at room temperature, Phys. Rev. B 86, 165205 (2012).
16. D.S. Gao, X.D. Gao, Y.Q. Wu, T.T. Zhang, J.N. Yang, X.M. Li, Epitaxial Co doped BaSnO3 thin films with tunable optical bandgap on MgO substrate, Applied Physics A (2019) 125:158
17. U. Kim, C. Park,1 T. Ha, R. Kim, H. S. Mun, H. M. Kim, H. J. Kim, T. H. Kim, N. Kim, J.Yu, K.H.Kim, J. H. Kim, K. Char, Dopant-site-dependent scattering by dislocations in epitaxial films of perovskite semiconductor $BaSnO_3$, APL Materials 2, 056107 (2014)
18. K. F. Moura, L.Chantellea, D. Rosendoa, E. Longob, I.M.G. Effect of Fe3+ Doping in the Photocatalytic Properties of $BaSnO_3$ Perovskitedos Santosa, Materials Research. 2017; 20(Suppl. 2): 317-324
19. K.Balamurugan, N.H.Kumar, J.A.Chelvane, P.N,Santhosh, Room temperature ferromagnetism in Fe-doped $BaSnO_3$, J. Alloys Compd. 472, 9–12 (2009)

20. M. Avinash, M. Muralidharan, K. Sivaji, Structural, optical and magnetic behaviour of Cr doped $BaSnO_3$ perovskite nanostructures, Physica B: Condensed matter 570 (2019), 157-165
21. M.R. Manju, V.P. Kumar, V. Dayal, Investigation of ferromagnetic properties in Fe/Co substituted $BaSnO_3$ perovskite stannates, Physica B 500 (2016) 14–19
22. K.K James, A. Aravind, M.K Jayaraj, Structural, optical and magnetic properties of Fe-doped barium stannate thin films grown by PLD, Appl. Surf. Sci. 282 (2013)121–5
23. M. Licheron, G. Jouan, E. Husson, J.Characterization of $BaSnO_3$ powder obtained by a modified sol-gel route, J Eur.Ceram. Soc. 17 (1997) 1453-1457.
24. P.H. Borse, U.A. Joshi, S. M. Ji, J. S. Jang, J. S. Lee. Band gap tuning of lead-substituted $BaSnO_3$ for visible light photocatalysis, Appl. Phys. Lett. 90, (2007) 034103
25. D. Fengtao, C. Bin, C. Hualei, N. Ruiyuan, C. Zhuo, Mater. Res. Bull. 44 (2009) 1930–1934
26. Li Hui Bi, Tang Wen Yi, Luo Juan Li, Xiao Ting, Li Wei Da, Hu, Yan Xiao, Min Yuan, Fabrication of porous $BaSnO_3$ hollow architectures using $BaCO_3$@SnO_2 core–shell nanorods as precursors, Appl. Surf. Sci. 257 (2010) 197-202
27. A.S. Deepa, S. Vidya, P.C. Manua, Sam Solomon, Annamma John, J.K. Thomas, Structural and optical characterization of $BaSnO_3$nanopowder synthesized through a novel combustion technique, J. Alloys Compd. 509 (2011) 1830–1835
28. E. Swatsitang, A.Karaphun, S. Phokha, T. Putjuso Characterization and magnetic properties of $BaSn_{1-x}Fe_xO_3$ nanoparticles prepared by a modified sol– gel method, J.Sci.Technol (2016) 77, 78–84
29. Toby, B. H., & Von Dreele, R. B. (2013). "GSAS-II: the genesis of a modern open-source all purpose crystallography software package". *Journal of Applied Crystallography*, **46**(2), 544-549.
30. S. Sumithra, N.V. Jaya, Band gap tuning and room temperature ferromagnetism in Co doped Zinc stannate nanostructures, Physica B 493, 35 (2016)
31. J.U. Brehm, M. Winterer, and H. Hahn, Synthesis and local structure of doped nanocrystalline zinc oxides, J.Appl. Phys. 100, 1 (2006).
32. S.Sumithra, N.V. Jaya, Structural, optical and magnetization studies of Fe-doped $CaSnO_3$ nanoparticles via hydrothermal route, J. Mater. Sci. Mater. Electron. 29, 4048 (2018).
33. M. Muralidharan, V. Anbarasu, A. E.Perumal, K. Sivakumar, Room temperature ferromagnetism in Cr doped $SrSnO_3$ perovskite system, J.Mater Sci: Mater Electron 28, (2017), 4125–4137
34. Lucena, G.L., Maia, A.S., Souza, A.G. Structural changes in Fe-doped $SrSnO_3$ perovskites during thermal analysis. J.Therm.Anal Calorim 115, (2014),137–144.275
35. S.A. Salehizadeh, H.M. Chenari, M. Shabani, H.A. Ahangar, R. Zamiri, A. Rebelo, J. S. Kumar, M.P.F.Graca, J.M.F. Ferreira, Structural and impedance spectroscopy characteristics of $BaCO_3$/$BaSnO_3$/SnO_2 nanocomposite: observation of a non-monotonic relaxation behavior RSC Adv.8, 2100 (2018). doi: 10.1039/c7ra12442b.

36. S.Sumithra, N.V. Jaya, Structural, optical and magnetization studies of Fe-doped $CaSnO_3$ nanoparticles via hydrothermal route, J.Mater. Sci. Mater. Electron. 29,4048 (2018).
37. J. Bohnemann, R. Libanori, M. Moreira, E. Longo, High-efficient microwave synthesis and characterization of SrSnO3 Chem. Eng. J. 155, (2009), 905–909
38. M.C.F. Alves, M.R. Nascimento, S.J.G. Lima, P.S. Pizani, J.W.M. Espinosa, E. Longo, L.E.B. Soledade, A.G. Souza, I.M.G.Santos, Influence of synthesis conditions on carbonate entrapment in perovskite $SrSnO_3$, Mater. Lett. 63, (2009), 118–120
39. Souza, A.E., Santos, G., Barra, B., Macedo, W.D. Jr., Teixeira, S.R., Santos, C.M., Longo, E.Photoluminescence of $SrTiO_3$: Influence of Particle Size and Morphology Cryst. Growth Des. 12(11), (2012), 5671–5679
40. M.R. Manju, K.S. Ajay, N.M. D'Souza, S. Hunagund, R.L. Hadimani, V. Dayal, Enhancement of Ferromagnetic Properties in Composites of $BaSnO_3$ and $CoFe_2O_4$, J. Magn. Magn. Mater. (2017)
41. S. H. Butt, M. S. Rafique, K. Siraj, A. Latif, A. Afzal, M. S. Awan, S. Bashir, N. Iqbal, Epitaxial thin-film growth of Ruddlesden–Popper-type $Ba_3Zr_2O_7$ from a $BaZrO_3$ target by pulsed laser deposition, Appl. Phys. A 122:658 (2016)
42. J. John, S. Suresh, S. R. Chalana, V. P. Mahadevan Pillai, Effect of substrate temperature, laser energy and post- deposition annealing on the structural, morphological and optical properties of laser-ablated perovskite $BaSnO_3$ films, Appl. Phys. A 125, (2019) 743.
43. W.Ahmad, D. Liu, W.Ahmad, Y. Wang, P. Zhang, T. Zhang, H. Zheng, Z. D. Chen, S. Li, Physisorption of Oxygen in SnO_2 Nanoparticles for Perovskite Solar Cells, IEEE J. Photovolt.9, (2019), 200-206
44. J. John, S.R. Chalana, R. Prabhu, V.P.M. Pillai, Effect of oxygen pressure on the structural and optical properties of $BaSnO_3$ films prepared by pulsed laser deposition method, Appl. Phys. A 125, (2019), 155.
45. J. Socratous, K.K. Banger, Y. Vaynzof, A. Sadhanala, A.D. Brown, A. Sepe, U. Steiner, H. Sirringhaus, Adv. Funct. Mater. (2015). https ://doi.org/10.1002/adfm.20140 4375
46. K. Lee, S. Shin, T. Degen, W.Lee, Y. S. Yoon, In situ analysis of SnO_2/Fe_2O_3/RGO to unravel the structural collapse mechanism and enhanced electrical conductivity for lithium-ion batteries Nano Energy, 32 (2017) 397–407
47. D.L Wood, J. Tauc, Weak absorption tails in amorphous semiconductors. Phys. Rev. B 5, (1972) 3144
48. M. Avinash, M. Muralidharan, K. Sivaji, Physica B: Condensed matter 570 (2019), 157-165
49. J John, M. Dhananjaya, S. Suresh, S. Savitha Pillai, M. Sahoo, O. M. Hussain,R.Philip, V. P. Mahadevan Pillai, Journal of Materials Science: Materials in Electronics (2020)
50. F. La Mattina, J.G. Bednorz, S.F. Alvarado, A. Shengelaya, K.A. Müller, H. Keller, Controlled oxygen vacancies and space correlation with Cr^{3+} in $SrTiO_3$ Phys. Rev. B 80, 075122 (2009)
51. G. Prathiba, S. Venkatesh, N.H. Kumar,Structural, magnetic and semiconducting

properties of Fe doped $SrSnO_3$ Solid State Commun. 150(31–32), 1436 (2010)
52. J.M.D Coey, M. Venkateshan, Donor impurity band exchange in dilute ferromagnetic oxides, Nat Mater 4, (2005) 173–179
53. F.T.G. Vieira, G.P. Casali, S.J.G. De Lima, M. SiuLi, E. Longo, A.D. Maia, A.G. Souza, I.M. Photoluminescence in $SrSnO_3:Fe^{3+}$ Perovskite Dos Santos, Curr. Phys. Chem. 4, 21 (2014)
54. A. Sarkar, S. K. De. Defect and Optical Properties of Sb doped and hydrogenated $BaSnO_3$, Semicond. Sci. Technol. 33, (2018), 035018
55. J.E.Wertz, J.R.Bolton, Electron Spin Resonance Elementary Theory and Practical Applications, first ed., New York,Chapman and Hall, 1986
56. J. Meng, Q. Lin, T. Chen, X. Wei, J. Li, Z. Zhang, Oxygen vacancy regulation on tungsten oxides with specific exposed facets for enhanced visible-lightdriven photocatalytic oxidation Nanoscale, 2018, 10, 2908-2915
57. V. Singh, G. Sivaramaiah, J.L. Rao, N. Singh, A.K. Srivastava, P.K. Singh, S.U. Pawar, H. Gao, P. Mardina, J. Combustion synthesized Fe doped CeO_2 powder-characterization, optical absorption and EPR spectroscopy Mater. Sci. 27, 4494 (2016)
58. I. Ardelean, P. Pascuta, L.V. Giurgiu, EPR and Magnetic Susceptibility Investigations of $Fe_2O_3B_2O_3$-KCl Glasses, Int. J. Mod. Phys. B 17, (2003), 3049
59. K.W. Wagner, Zur theorie der unvollkommenen dielektrika, Annalen der Physik 345 (5) (1913) 817-855
60. I. Gul, A. Abbasi, F. Amin, M. Anis-ur-Rehman, A. Maqsood, Structural, magnetic and electrical properties of $Co_{1-x}Zn_xFe_2O_4$ synthesized by co-precipitation method, Journal of magnetism and magnetic materials 311 (2) (2007) 494-499
61. S. Sharma, K.Nanda, R.S. Kundu, R. Punia, N. Kishore, Journal of Atomic, Molecular, Condensate & Nano Physics, (2015) 15–31
62. M.M. Hassan, A.S.Ahmed, M.Chaman, WasiKhan, A.H.Naqvi, A.Azam, Structural and frequency dependent dielectric properties of Fe3+ doped ZnO nanoparticles Materials Research Bulletin 47, (2012) 3952–3958 268
63. S. A.Ansari, A. Nisar, B. Fatma, W. Khan, A.H. Naqvi, Investigation on structural, optical and dielectric properties of Co doped ZnO nanoparticles synthesized by gel-combustion route, Material Science and Engineering B,177, 428-435 (2012)
64. R. Zamiri, A. Kaushal, A. Rebelo, J.M.F. Ferreira, Ceramics International,40,1635-1639, (2013), http://dx.doi.org/10.1016/j.ceramint.2013.07.054

Figures

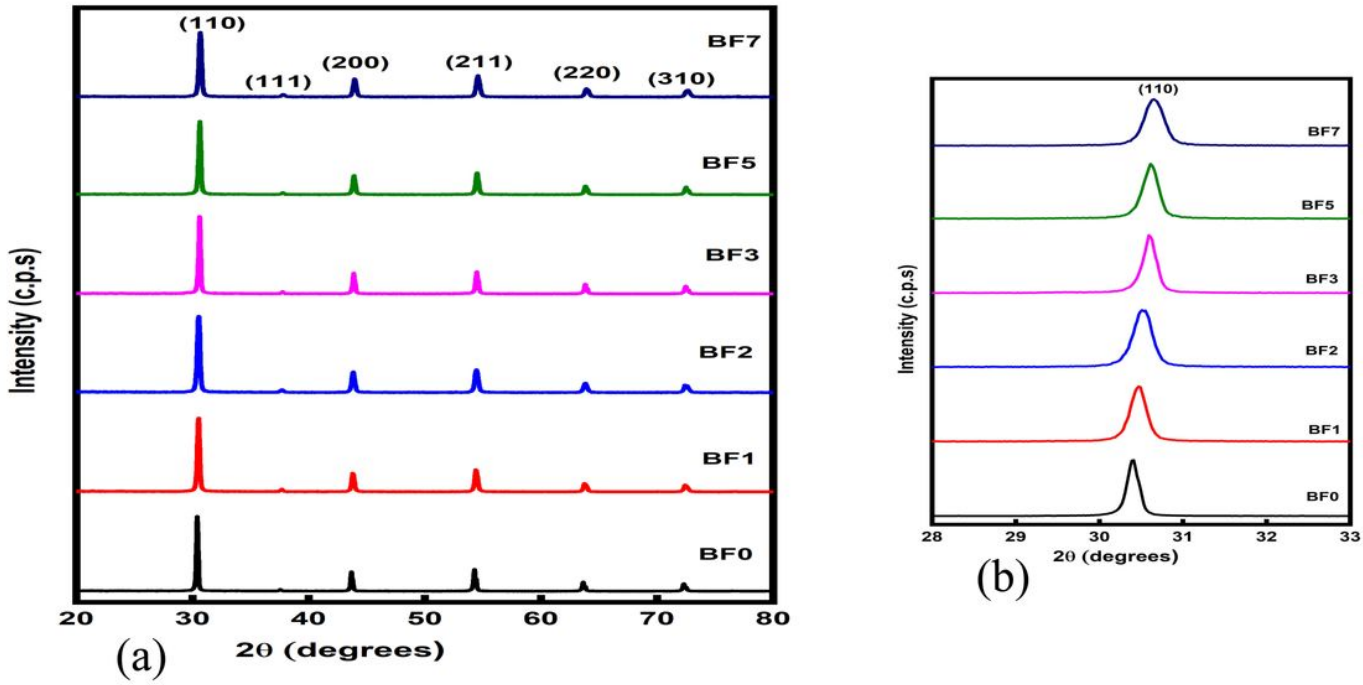

Figure 1

(a) XRD patterns of the BaSn1-xFexO3 (x=0.00, 0.01, 0.02, 0.03, 0.05 and 0.07) samples (b) The shift of (110) peak as a function Fe doping concentration of the BaSn1-xFexO3 samples

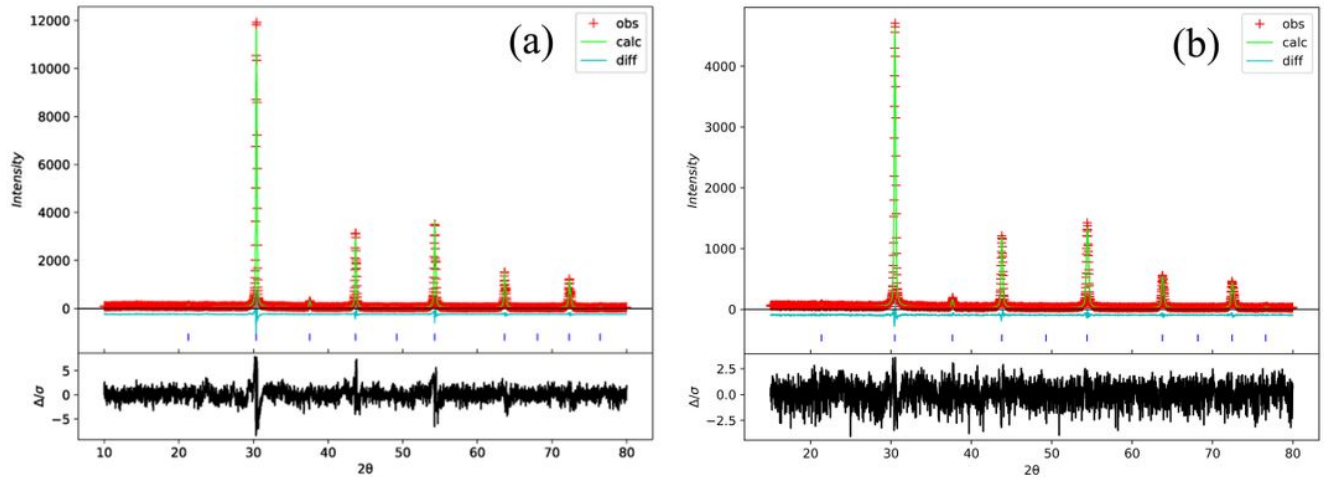

Figure 2

Rietveld refinement of pure and Fe doped BaSnO3 samples

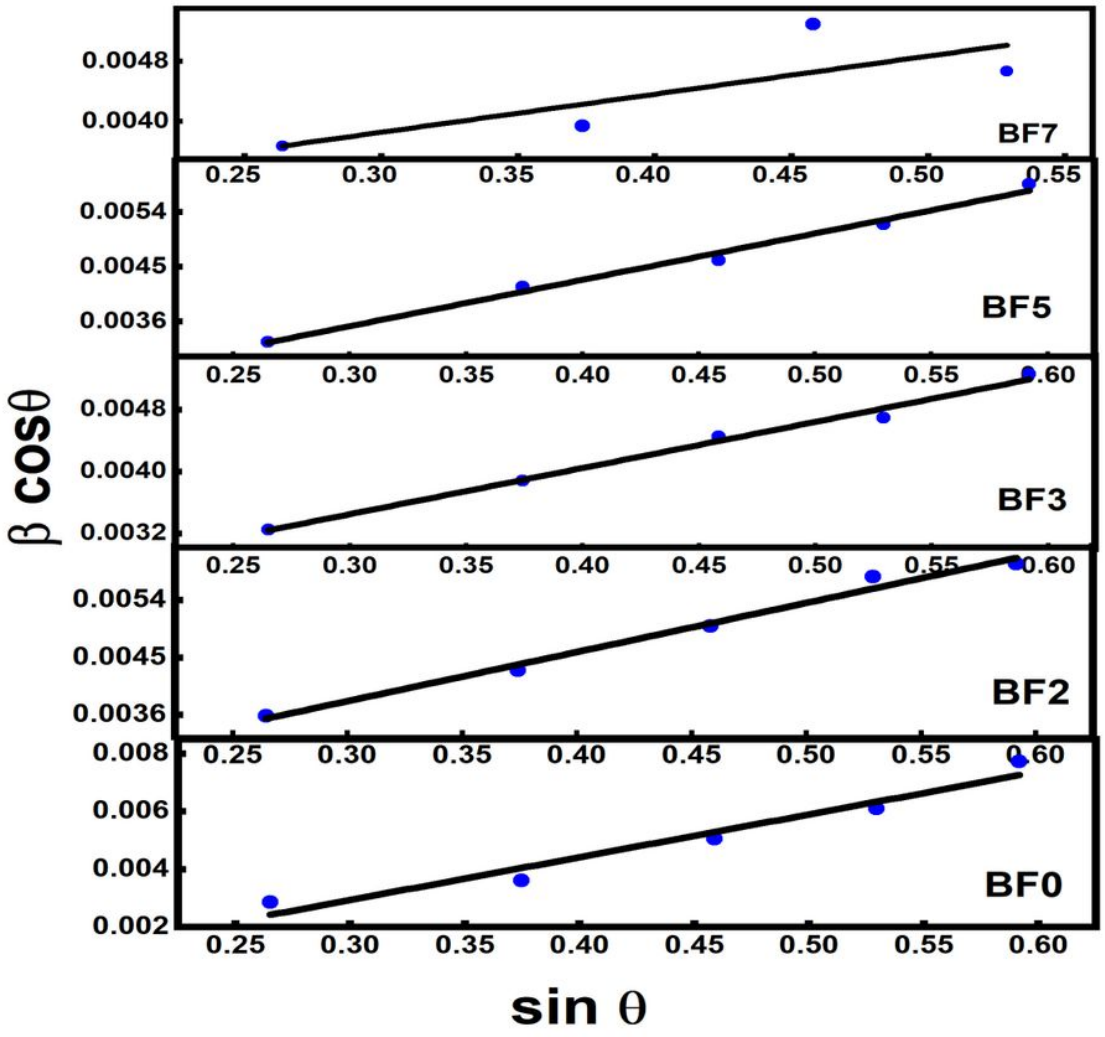

Figure 3

Williamson–Hall plot of pure BaSnO3 and Fe doped BaSnO3 samples

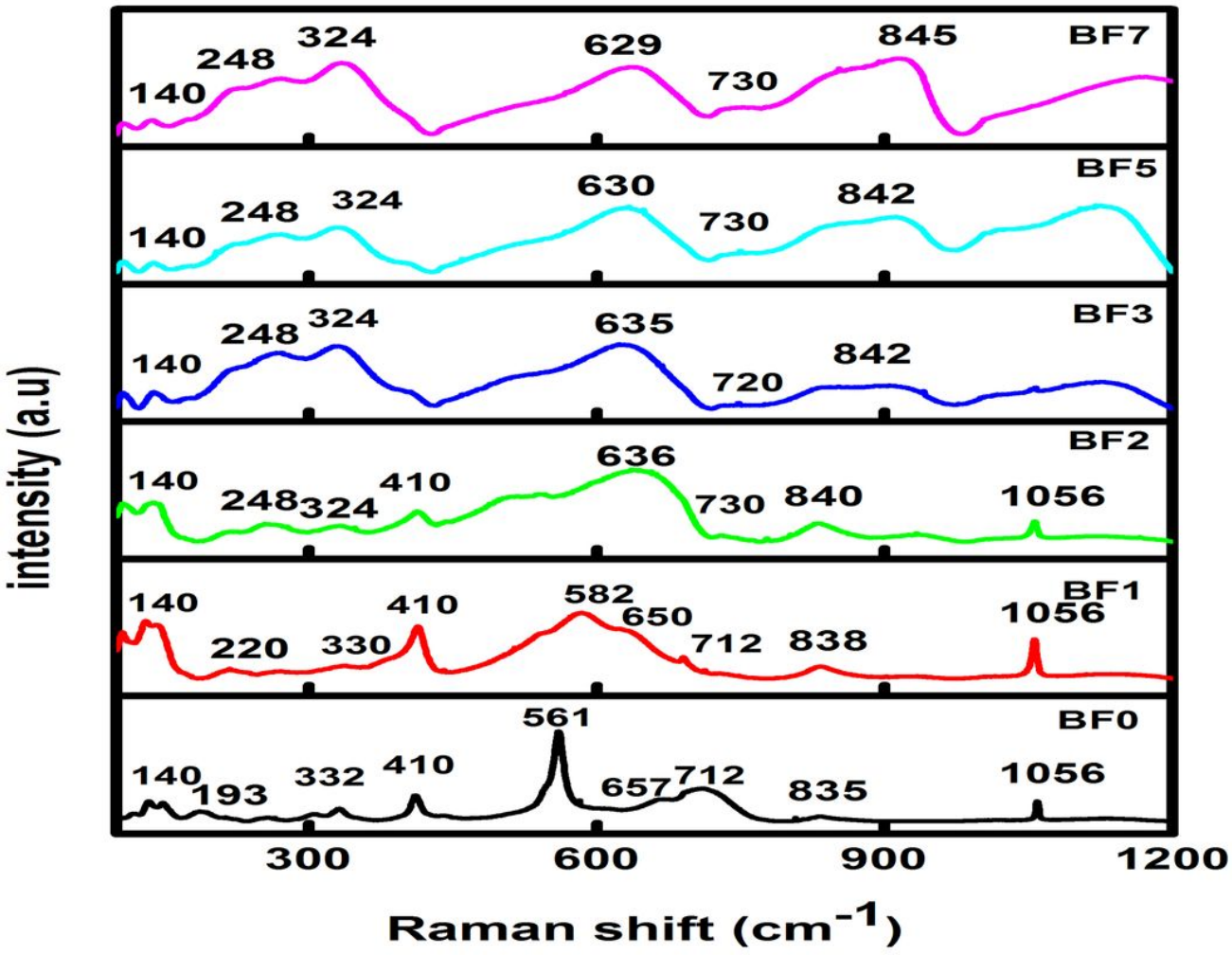

Figure 4

Micro-Raman spectra of pure BaSnO3 and Fe doped BaSnO3 samples

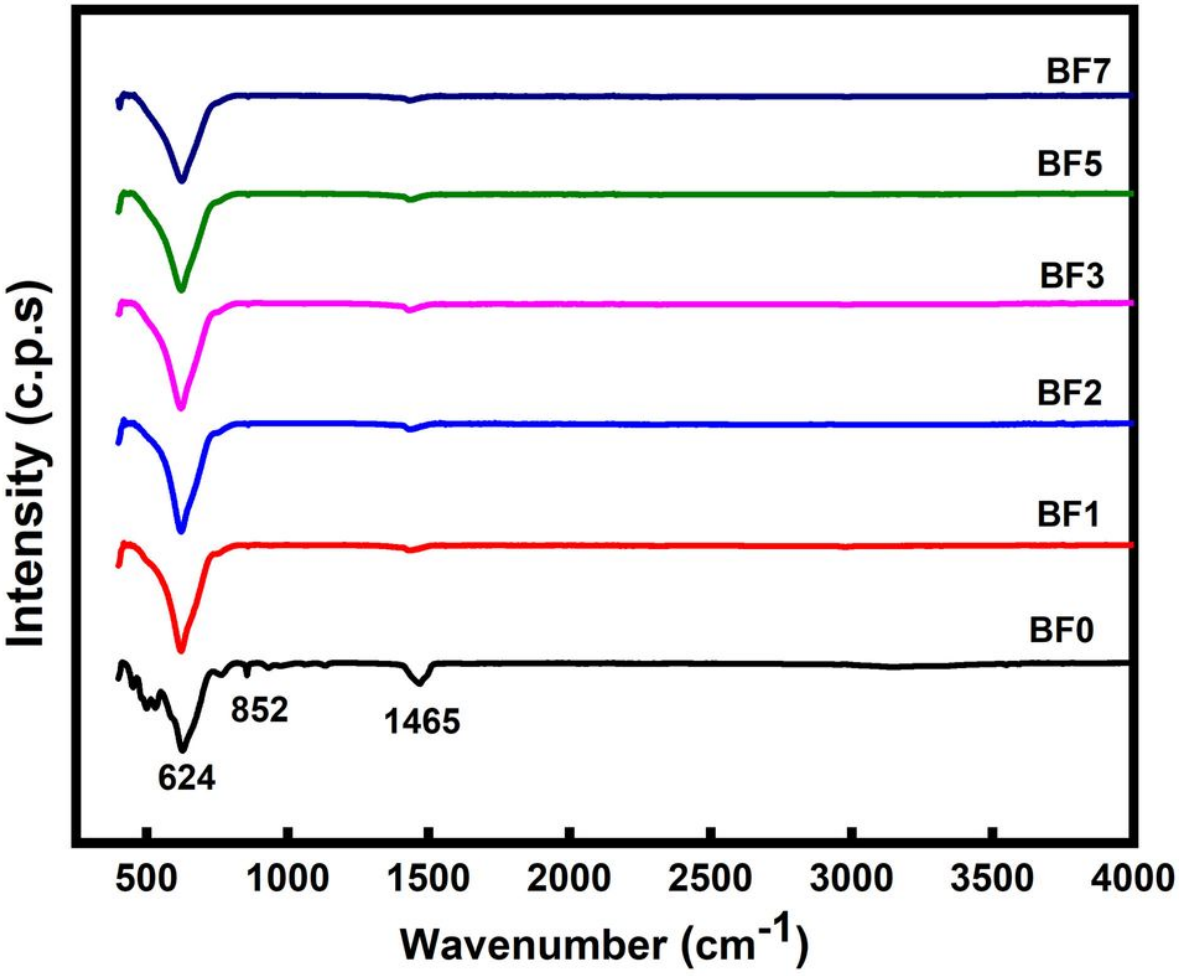

Figure 5

FTIR spectra of pure BaSnO3 and Fe doped BaSnO3 samples

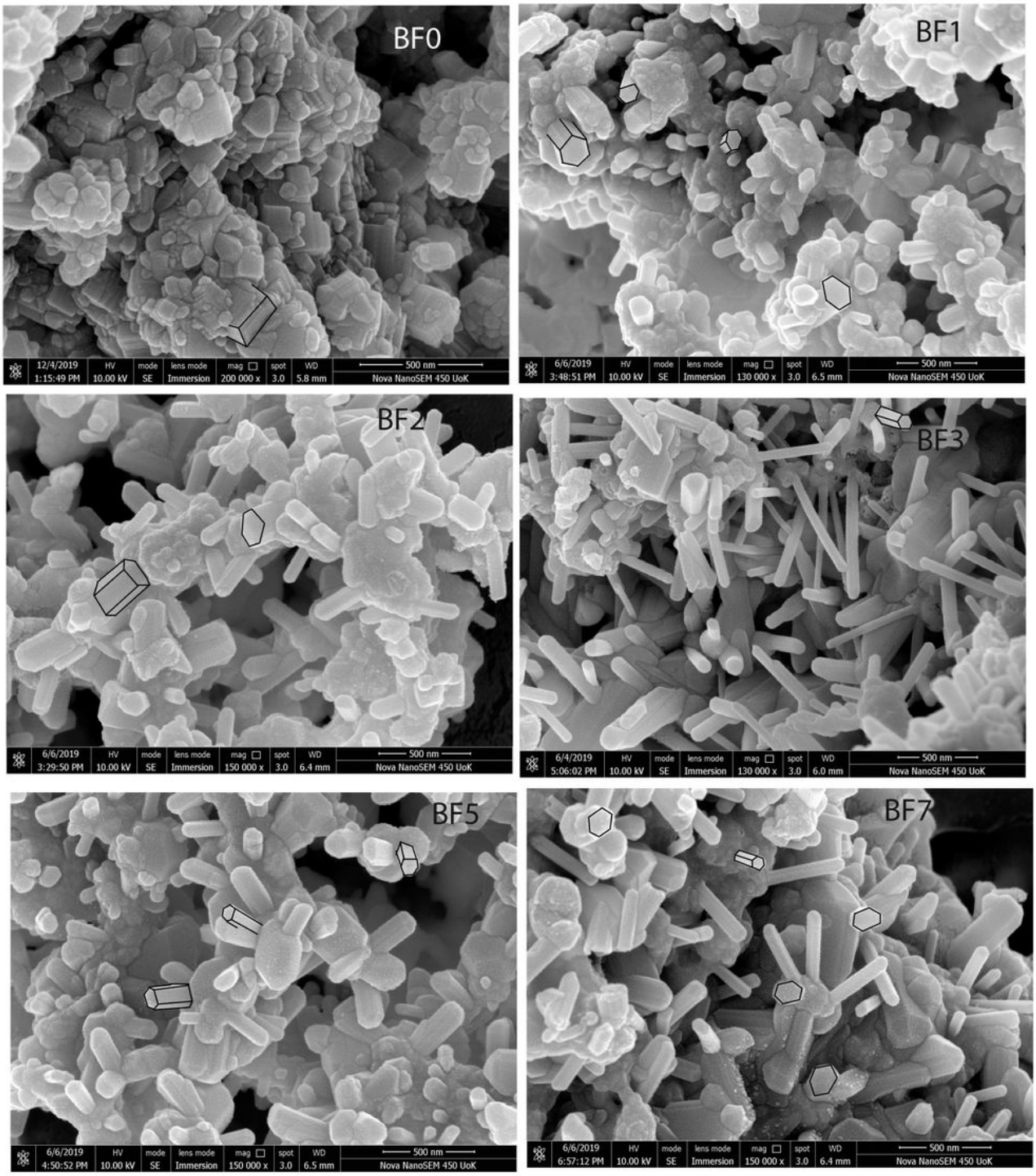

Figure 6

FESEM of pure and Fe-doped BaSnO3 samples

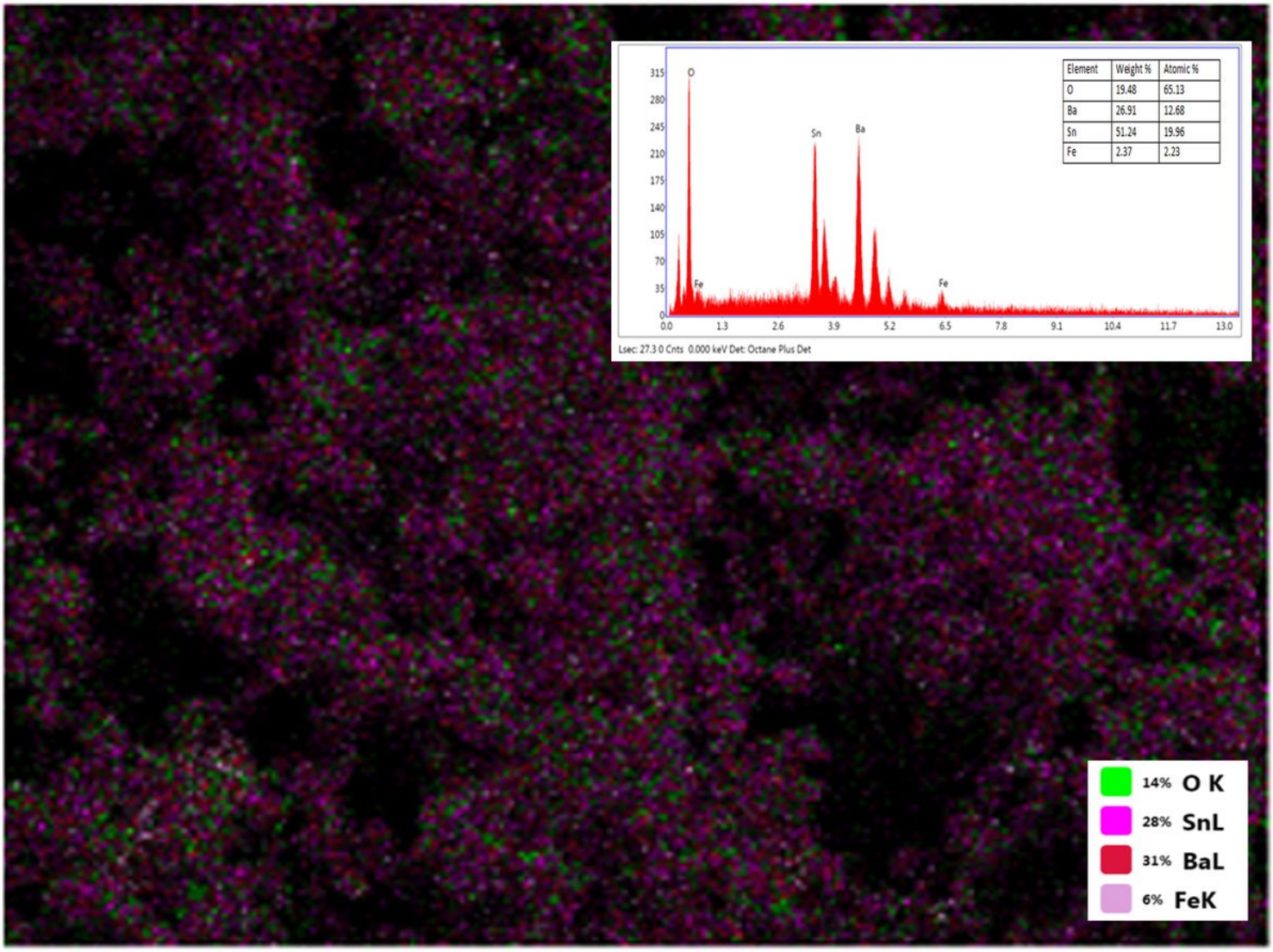

Figure 7

EDS mapping and spectra of BF3 sample

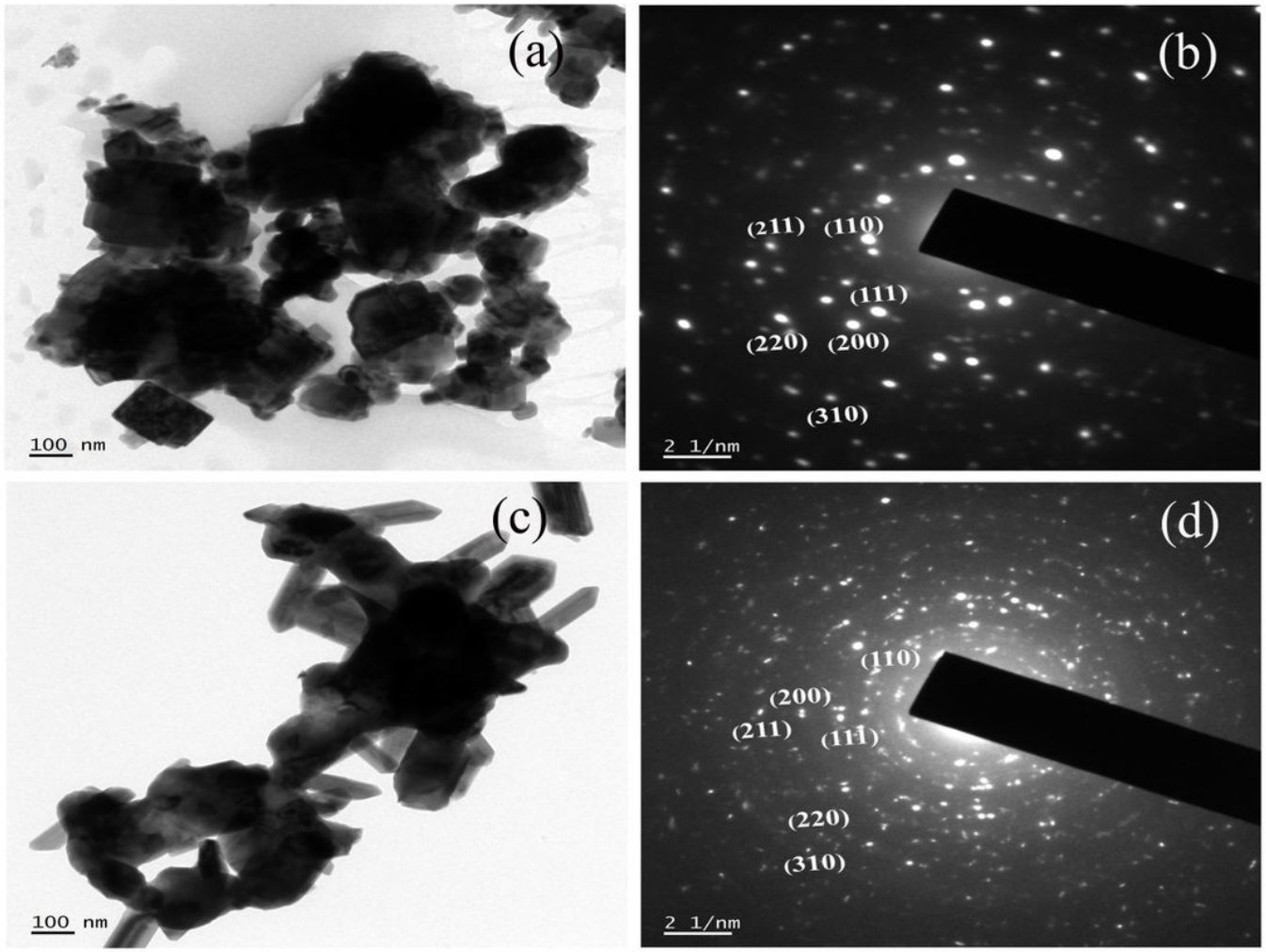

Figure 8

(a), (c) TEM images, (b) and (d) SAED pattern of pure and Fe doped BaSnO3 (BF3) samples

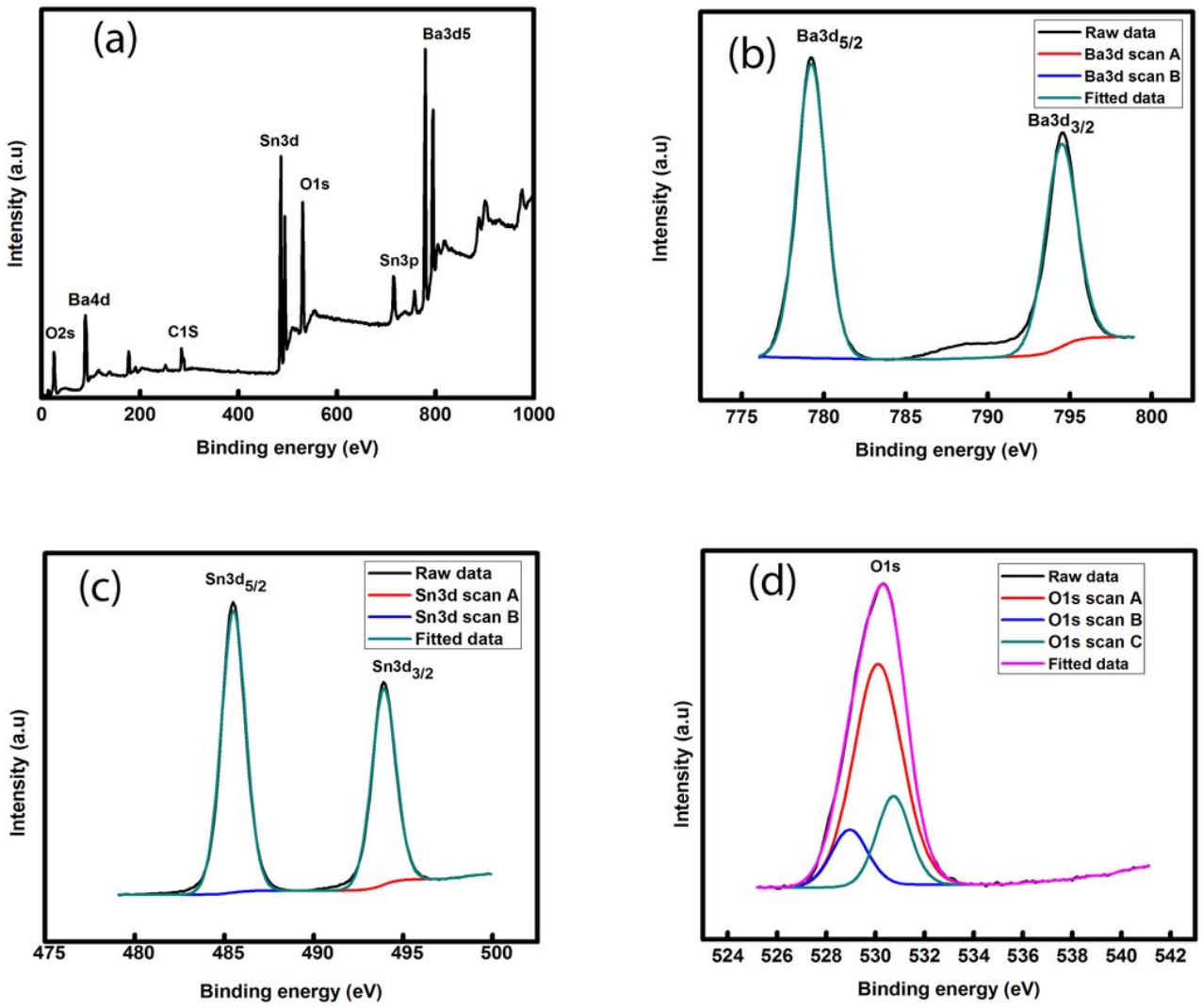

Figure 9

XPS analysis of pure BaSnO3 powder sample (a). XPS survey spectrum (b). core level splitting of peaks of Ba (c). the core level splitting of peaks of Sn and (d). the core level splitting of peaks of O.

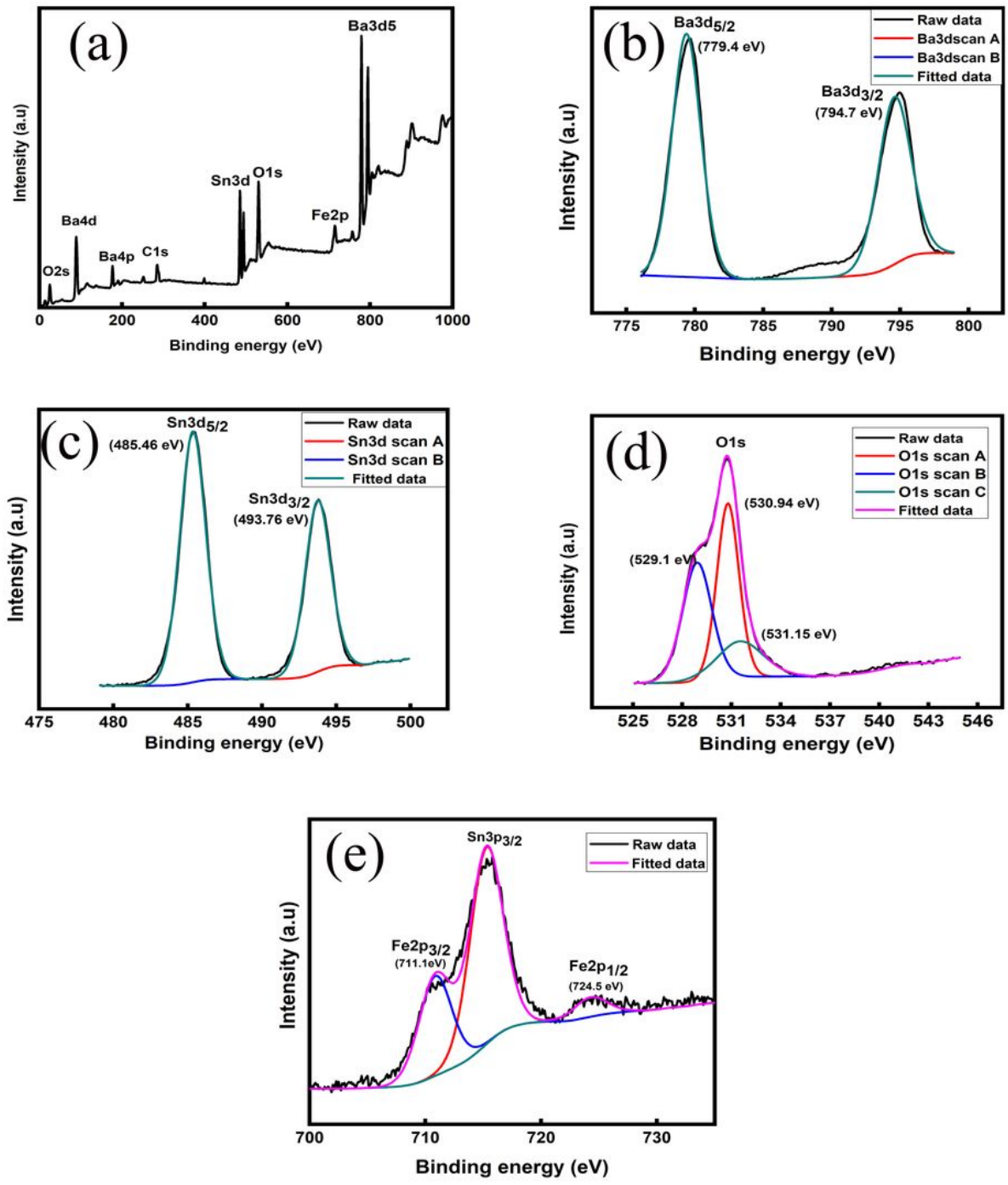

Figure 10

XPS analysis of Fe doped BaSnO3 (BF3) powder (a). XPS survey spectrum (b). core level splitting of peaks of Ba (c). core level splitting of peaks of Sn (c). core level splitting of peaks of Oand (d).core level splitting of peaks of Fe.

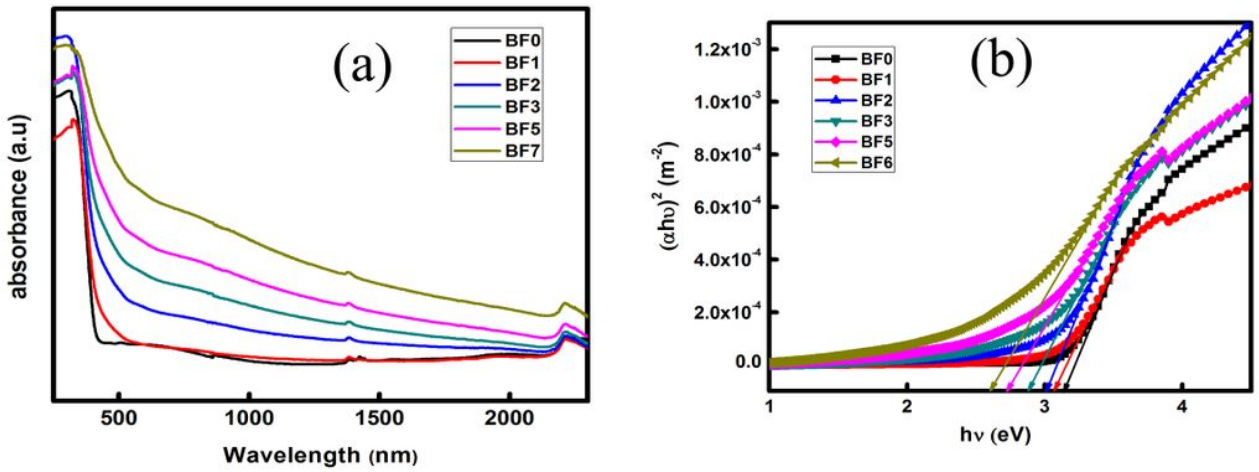

Figure 11

(a) Absorption spectra and (b) Tauc plot of pure and Fe-doped BaSnO3 samples

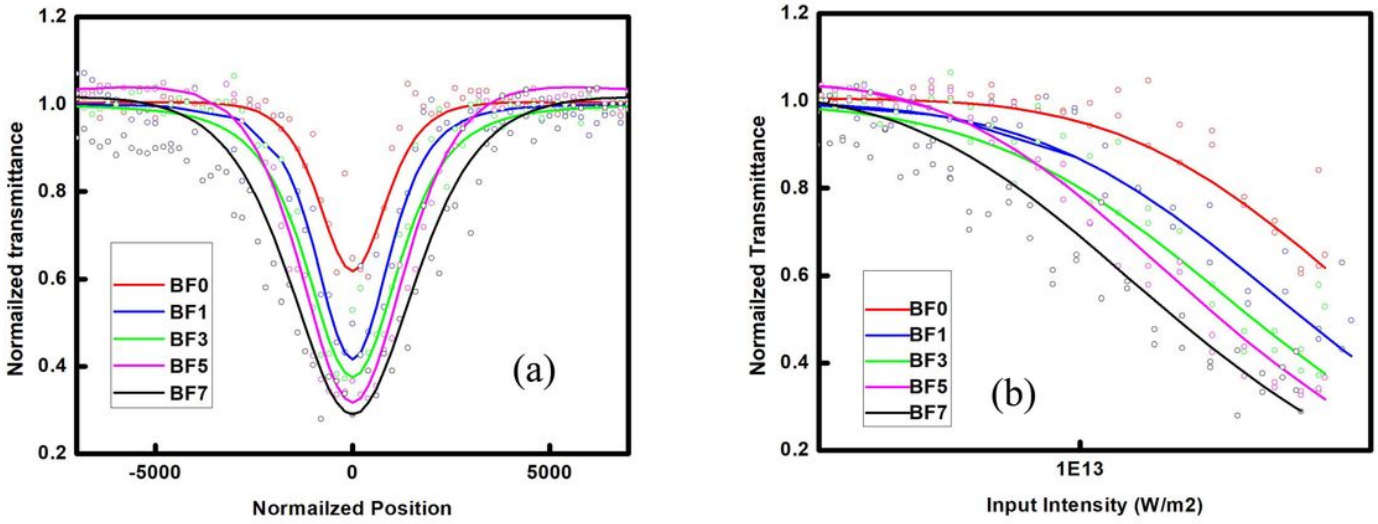

Figure 12

(a) Open-aperture Z-scan curves measured for pure and Fe doped BaSnO3 samples. (b) The normalized transmittance calculated as a function of input intensity. Symbols are data points while solid curves are numerical fits calculated using equation 5.

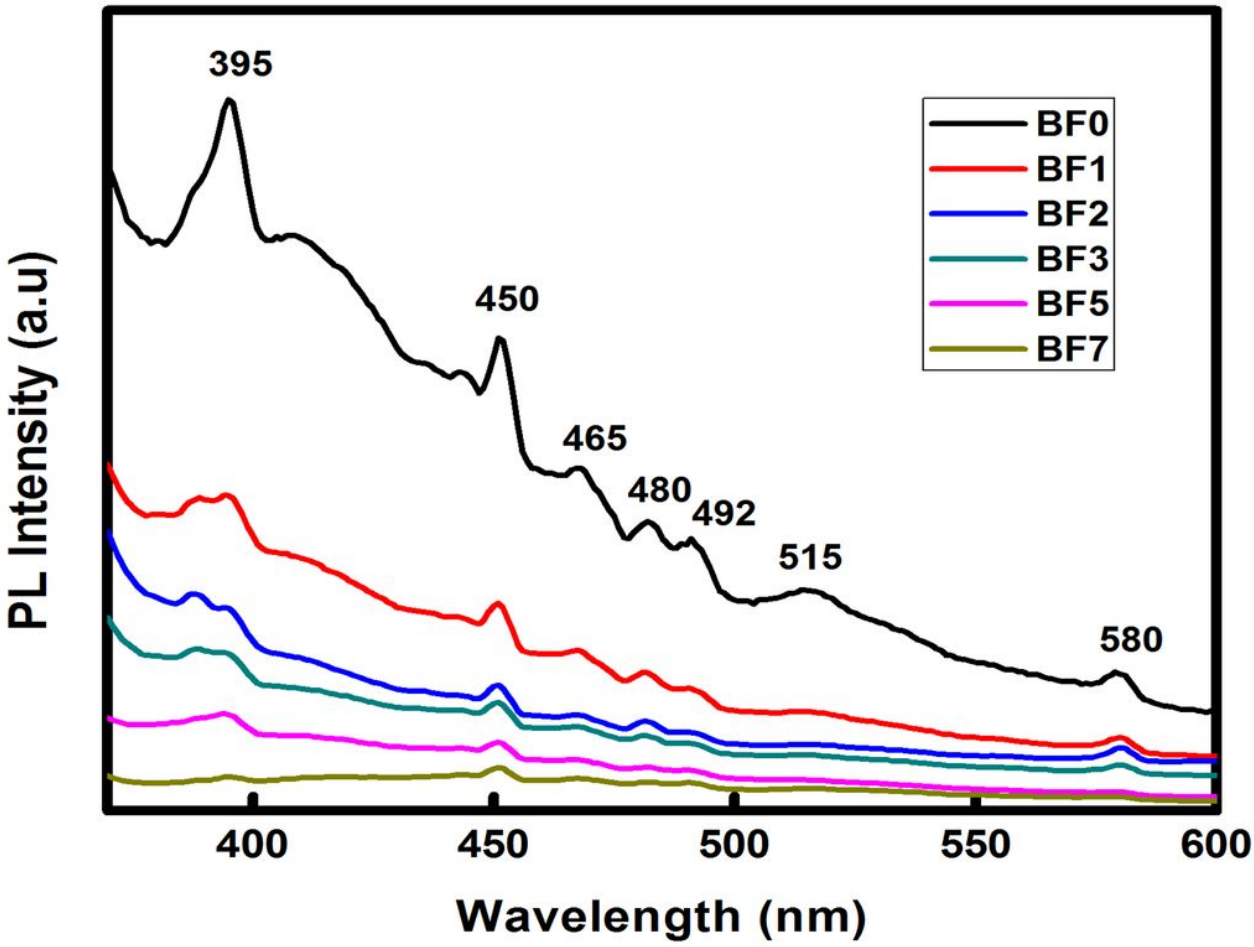

Figure 13

PL spectra of pure and Fe doped BaSnO3 powder samples with different Fe dopant concentration

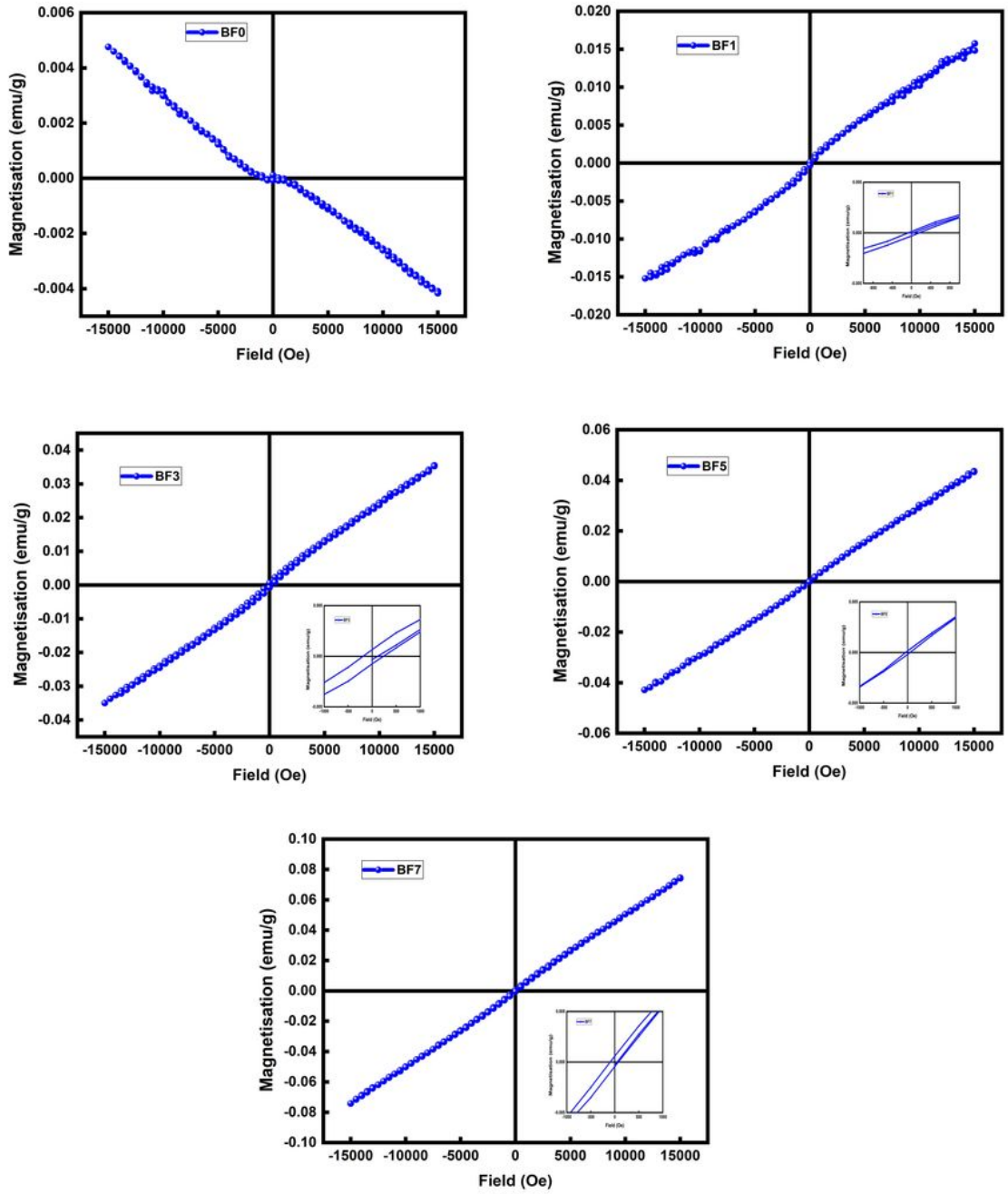

Figure 14

M-H curve of pure and Fe-doped BaSnO3 at T= 300K

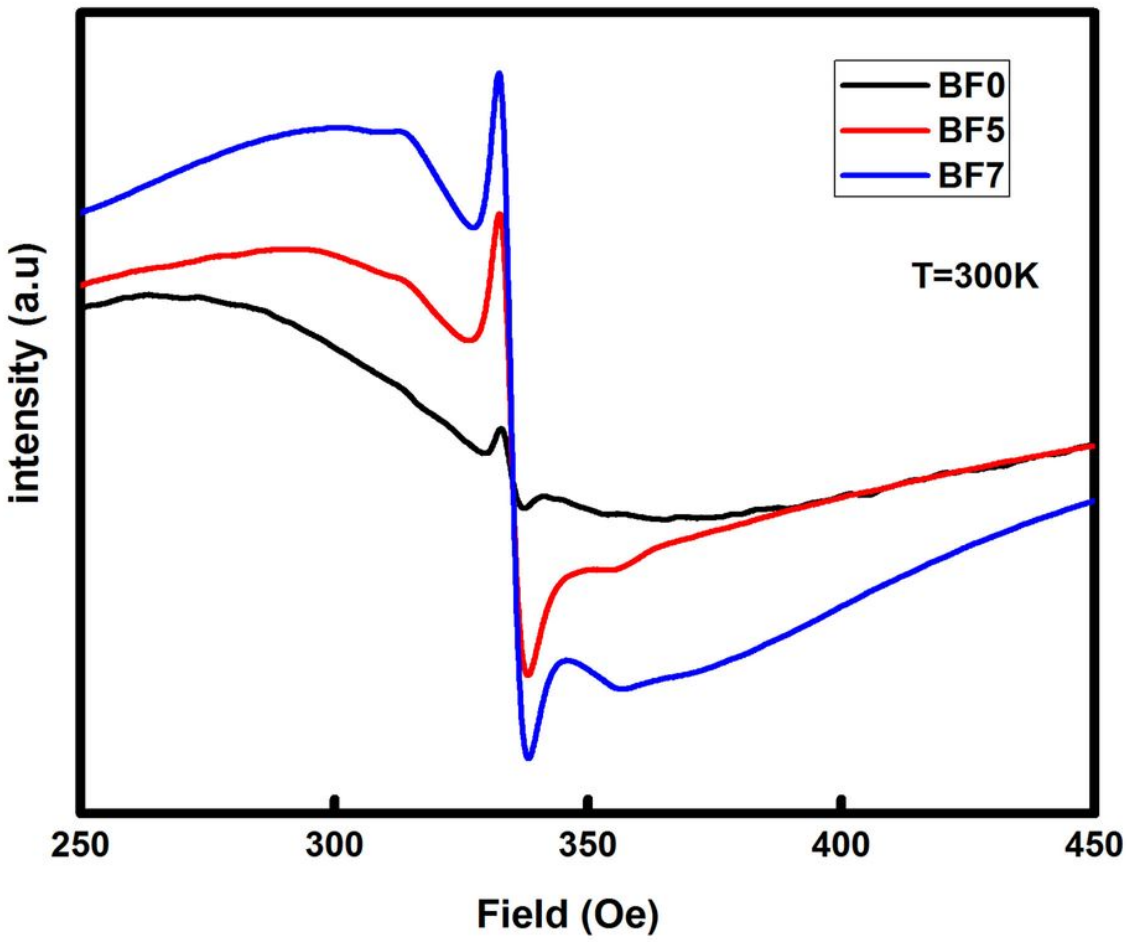

Figure 15

EPR spectra of pure and Mn-doped BaSnO3 samples

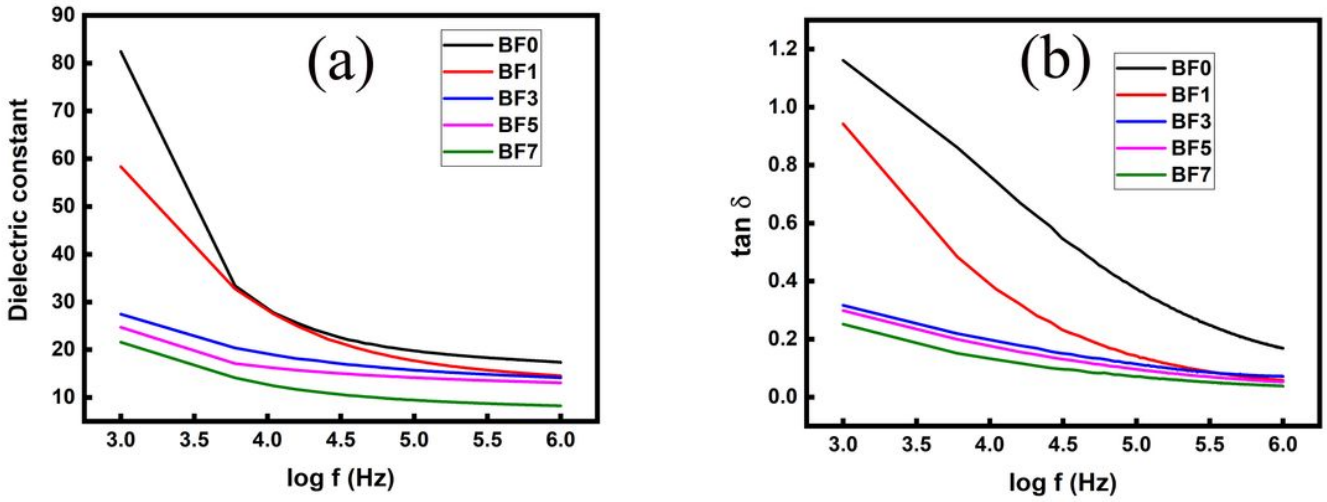

Figure 16

Variation of (a) dielectric constant (b) loss tangent for pure and Fe doped BaSnO3

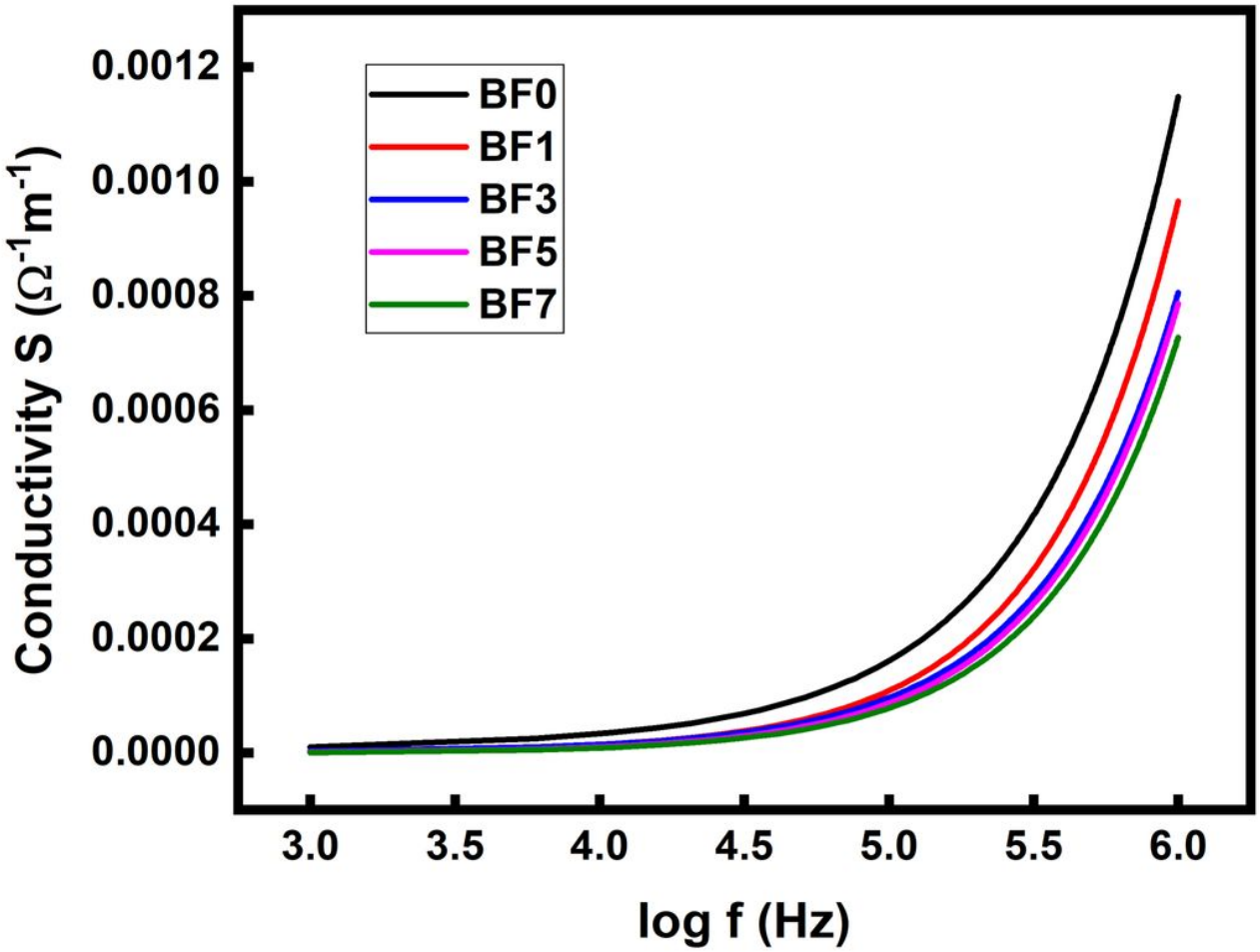

Figure 17

Variation in ac conductivity of pure and Fe doped BaSnO3 with frequency